1.0

4.5
5.0
5.6

2.8

2.5

3.2

2.2

3.6

4.0

2.0

1.1

1.8

1.25

1.4

1.6

MICROCOPY RESOLUTION TEST CHART
NATIONAL BUREAU OF STANDARDS-1963-A

ADA042547

DNA 4149F

LABORATORY INVESTIGATION OF STEMMING AND CONTAINMENT IN UNDERGROUND NUCLEAR TESTS

Stanford Research Institute

333 Ravenswood Avenue

Menlo Park, California 94025

October 1976

Final Report

CONTRACT No. DNA 001-75-C-0083

APPROVED FOR PUBLIC RELEASE;
DISTRIBUTION UNLIMITED.

D D C

AUG 5 1977

C

DDC FILE COPY

Prepared for
Director
DEFENSE NUCLEAR AGENCY
Washington, D. C. 20305

REPORT DOCUMENTATION PAGE		READ INSTRUCTIONS BEFORE COMPLETING FORM
1. REPORT NUMBER DNA 4149F	2. GOVT ACCESSION NO.	3. RECIPIENT'S CATALOG NUMBER
4. TITLE (and Subtitle) LABORATORY INVESTIGATION OF STEMMING AND CONTAINMENT IN UNDERGROUND NUCLEAR TESTS		5. TYPE OF REPORT & PERIOD COVERED Final Report.
		6. PERFORMING ORG. REPORT NUMBER SRI Project PYU-3702
7. AUTHOR(s) A. L. Florence		8. CONTRACT OR GRANT NUMBER(s) DNA 001-75-C-0083
9. PERFORMING ORGANIZATION NAME AND ADDRESS Stanford Research Institute 333 Ravenswood Avenue Menlo Park, California 94025		10. PROGRAM ELEMENT, PROJECT, TASK AREA & WORK UNIT NUMBERS Subtask J24AAXYS984-26
11. CONTROLLING OFFICE NAME AND ADDRESS Director Defense Nuclear Agency Washington, D.C. 20305		12. REPORT DATE October 1976
		13. NUMBER OF PAGES 90 88p.
14. MONITORING AGENCY NAME & ADDRESS(if different from Controlling Office)		15. SECURITY CLASS (of this report) UNCLASSIFIED
		15a. DECLASSIFICATION/DOWNGRADING SCHEDULE

16. DISTRIBUTION STATEMENT (of this Report)

Approved for public release; distribution unlimited.

17. DISTRIBUTION STATEMENT (of the abstract entered in Block 20, if different from Report)

18. SUPPLEMENTARY NOTES

This work sponsored by the Defense Nuclear Agency under RDT&E RMSS Code B344075462 J24AAXYS98426 H2590D.

19. KEY WORDS (Continue on reverse side if necessary and identify by block number)

Stemming	Containment
Extrusion	Cavity
Nuclear	Hydrofracture
Underground	

20. ABSTRACT (Continue on reverse side if necessary and identify by block number)

As part of the DNA stemming and containment program for underground nuclear testing, laboratory investigations were carried out in three areas: generation of experimental results suitable for correlation with predictions of computer codes used in DNA grout flow calculations, development of a containment experiment for studying residual stress fields around exploded cavities, and a theoretical analysis for studying the residual stress fields. Grout flow results were generated and supplied in a form suitable for code

DD FORM 1473 EDITION OF 1 NOV 65 IS OBSOLETE
1 JAN 73

20.   ABSTRACT   (Continued)

correlation.   The containment experiment was brought to an advanced stage of development.   The theoretical analysis, based on many simplifying assumptions, was completed up to the second cavity expansion stage, resulting in a reasonable description of the stress field formation.

ACCESSION for
NTIS   White Section ☑
DDC   Buff Section   ☐
UNANNOUNCED   ☐
JUSTIFICATION

BY
DISTRIBUTION/AVAILABILITY CODES
Dist.   SPECIAL

A

SUMMARY

The purpose of this project is to conduct laboratory investigations
in support of the DNA stemming and containment program for underground
nuclear tests.

Over the years, the DNA stemming and containment program has con-
sisted of five main parts:

(1) Code development and application for ground motion,
    tunnel closure, and grout flow calculations.

(2) Material properties determination.

(3) Laboratory investigations.

(4) Scaled high explosive tests.

(5) Field diagnostics.

SRI has been conducting the laboratory investigations.

During this phase of the laboratory program, experimental results
were generated for correlation with grout flow code predictions, a con-
tainment experiment was developed to study the residual stress surrounding
an exploded cavity in a rheological material, and a simple analysis was
performed to describe the formation of the residual stress field.

A dynamic grout extrusion technique was used to generate results
suitable for correlation with grout flow code predictions. With this
technique, a cylindrical specimen of superlean grout (SLG) in a heavy
steel tube is extruded into a coaxial transparent tunnel of smaller dia-
meter by a steel piston. The piston is driven by a well defined pressure
pulse and the motion of the piston and SLG front is observed by high speed
camera. Colored ceramic beads are embedded in the grout to observe the
initial and final positions of an array of particles. An auxiliary experi-
ment was devised and used twice to obtain the friction between SLG under
pressure and the steel container walls. Properties of the grout were

determined. Recommended improvements to the technique are more precise control over the grout properties and further friction experiments to establish reliability and dependence on pressure and velocity.

In the containment experiment, a small spherical charge is cast in a sphere of rock matching grout (RMG) with properties similar to those of Nevada Test Site tuff. The RMG sphere is hydraulically pressurized to represent overburden. The explosive is detonated and the residual gases released by drilling into the cavity. Dyed glycerol fluid is pumped into the cavity at a constant flow rate until fracture occurs and a steady radial pressure gradient is established. The internal pressure is removed and then the external pressure is removed. The cracked sphere is drained and tapped into two parts by use of a chisel, and each exposed fracture plane is photographed. The main observations of this work are

- Hydrofracture pressures in an exploded cavity were 50% higher than those in an unexploded cavity.

- Existence of a residual stress field was demonstrated by the increased hydrofracture pressure and by fracture patterns.

- Permeability was decreased by the explosion.

- Reproducibility of the hydrofracture experiments with an unexploded cavity was good.

- Further work is required to demonstrate reproducibility of hydrofracture experiments with an exploded cavity.

In the containment analysis, a gas with a known equation of state is assumed to instantaneously pressurize a spherical cavity in a solid homogeneous and isotropic medium. The analysis was rendered tractable by the following idealizations:

- Incompressibility
- Elastic-perfectly plastic behavior
- Yielding by the Mises condition
- Plastic straining by the associated flow rule.

2

Overburden is included as a constant pressure infinitely far from the cavity. Numerical examples are used to describe cavity expansion and formation of the residual stress field. Predictions generally agree with the predictions of finite-difference codes; cavity expansion agrees with the containment experiment. Formulas were derived for estimates of cavity expansion and maximum residual stresses and their locations. The next step in the analysis is to incorporate a yield condition that is stronger in compression than tension to make the analysis more representative of rheological materials.

PREFACE

The authors are indebted to the technical monitor, Carl Keller (DNA FTD) for ideas and guidance, to members of the containment community for helpful suggestions, to Scott Butters and Dan Gardener of Terra Tek, Inc. for material property determination, and to George Abrahamson for overall project supervision.

Table

CONVERSION FACTORS FOR U.S. CUSTOMARY TO METRIC (SI) UNITS OF MEASUREMENT

To Convert From	To	Multiply By
angstrom	meters (m)	$1.000\ 000 \times E\ -10$
atmosphere (normal)	kilo pascal (kPa)	$1.013\ 25 \times E\ +2$
bar	kilo pascal (kPa)	$1.000\ 000 \times E\ +2$
barn	meter^2 (m^2)	$1.000\ 000 \times E\ -28$
British thermal unit (thermochemical)	joule (J)	$1.054\ 350 \times E\ +3$
calorie (thermochemical)	joule (J)	$4.184\ 000$
cal (thermochemical)/cm^2	mega joule/m^2 (MJ/m^2)	$4.184\ 000 \times E\ -2$
curie	giga becquerel (GBq)*	$3.700\ 000 \times E\ +1$
degree (angle)	radian (rad)	$1.745\ 329 \times E\ -2$
degree Fahrenheit	degree kelvin (K)	$t_k = (t°f + 459.67)/1.8$
electron volt	joule (J)	$1.602\ 19 \times E\ -19$
erg	joule (J)	$1.000\ 000 \times E\ -7$
erg second	watt (W)	$1.000\ 000 \times E\ -7$
foot	meter (m)	$3.048\ 000 \times E\ -1$
foot-pound-force	joule (J)	$1.355\ 818$
gallon (U.S. liquid)	meter^3 (m^3)	$3.785\ 412 \times E\ -3$
inch	meter (m)	$2.540\ 000 \times E\ -2$
jerk	joule (J)	$1.000\ 000 \times E\ +9$
joule/kilogram (J/kg) (radiation dose absorbed)	Gray (Gy)	$1.000\ 000$
kilotons	terajoules	4.183
kip (1000 lbf)	newton (N)	$4.448\ 222 \times E\ +3$
kip/inch^2 (ksi)	kilo pascal (kPa)	$6.894\ 757 \times E\ +3$
ktap	newton-second/m^2 (N-s/m^2)	$1.000\ 000 \times E\ +2$
micron	meter (m)	$1.000\ 000 \times E\ -6$
mil	meter (m)	$2.540\ 000 \times E\ -5$
mile (international)	meter (m)	$1.609\ 344 \times E\ +3$
ounce	kilogram (kg)	$2.834\ 952 \times E\ -2$
pound-force (lbf avoirdupois)	newton (N)	$4.448\ 222$
pound-force inch	newton-meter (N-m)	$1.129\ 848 \times E\ -1$
pound-force/inch	newton/meter (N/m)	$1.751\ 268 \times E\ +2$
pound-force/foot^2	kilo pascal (kPa)	$4.788\ 026 \times E\ -2$
pound-force/inch^2 (psi)	kilo pascal (kPa)	$6.894\ 757$
pound-mass (lbm avoirdupois)	kilogram (kg)	$4.535\ 924 \times E\ -1$
pound-mass-foot^2 (moment of inertia)	kilogram-meter^2 (kg/m^2)	$4.214\ 011 \times E\ -2$
pound-mass/foot^3	kilogram/meter^3 (kg/m^3)	$1.601\ 846 \times E\ +1$
rad (radiation dose absorbed)	Gray (Gy)$^+$	$1.000\ 000 \times E\ -2$
roentgen	coulomb/kilogram (C/kg)	$2.579\ 760 \times E\ -4$
shake	second (s)	$1.000\ 000 \times E\ -8$
slug	kilogram (kg)	$1.459\ 390 \times E\ +1$
torr (mm Hg, 0°C)	kilo pascal (kPa)	$1.333\ 22 \times E\ -1$

*The becquerel (Bq) is the SI unit of radioactivity; 1 Bq = 1 event/s.

$^+$The Gray (Gy) is the SI unit of absorbed radiation.

TABLE OF CONTENTS

LIST OF ILLUSTRATIONS

LIST OF ILLUSTRATIONS (Continued)

LIST OF ILLUSTRATIONS (Continued)

LIST OF TABLES

I   INTRODUCTION

During an underground nuclear explosion, the burst of radiation that travels along a steel line-of-sight vacuum pipe to the test stations is followed by ground shock collapse of the pipe. Energy flow from the source and the violent pipe collapse form a plasma jet, which must be stopped before the plasma can reach the test stations and damage the experiments. Devices like mufflers and doors delay the plasma so that the ground shock can seal the pipe ahead of it. The tunnel space around the pipe is filled with grout to provide mechanical coupling, so that, on closure, the tunnel becomes filled with grout and broken-up pipe. The ground motion ceases more rapidly than the grout motion so that grout continues to flow along the tunnel for some time. This grout flow is also aided by the gas pressure in the device cavity. In a successful stemming scheme, this late-time extrusion is halted before the grout reached the test stations.

The spherically diverging ground motion is eventually brought to rest by outward energy radiation of stress waves, energy dissipation of crushing, distortion, and crack formation, and the combined resistance of tensile tangential stresses and overburden pressure. This combined resistance eventually causes a rebound of the medium that may cause further plastic work around the cavity and intensify the residual stress field.

In underground nuclear tests, it is required that radioactive gases not be released into the atmosphere. In general, this requirement will be met if experimental tunnels leading from the nuclear device cavity are stemmed successfully and if the residual cavity gases are contained by the adjacent surrounding medium. The residual stress field created around the cavity by the explosion probably aids containment. Although containment has been achieved for many years and stemming has generally been successful in recent nuclear tests, reliability is uncertain and planned tests still require extensive containment evaluation.

11

Over the years, the DNA stemming and containment (SAC) program has consisted of five main parts: code development for ground motion, tunnel closure, and grout flow calculations, material properties determination, laboratory investigations, scaled high explosive tests, and field diagnostics. SRI has been conducting the laboratory investigations.[1-4]

Our laboratory investigations during the last year are completely documented in Topical Reports 3702-1, 3702-2, 3702-3, and 3702-4. This report serves to summarize our findings. The areas of research summarized in Section II are dynamic grout extrusion experiments (Topical Report 3702-4),[5] experiments developed to study the residual stress field surrounding an exploded cavity (Topical Report 3702-3),[6] and a simple analysis performed to describe the formation of the residual stress field (Topical Report 3702-2).[7] Sections III, IV, and V of this report summarize the developmental progress and the principal results obtained.

At the start of this year's work, photoplasticity was considered for investigating residual stress fields caused by the dynamic expansion of holes and cavities. The work led to the conclusion that the method is unsuitable and is described in SRI Topical Report 3702-1.[8]

II   LABORATORY PROGRAM

The three main areas of the ongoing SAC laboratory study are

- Dynamic SLG extrusion experiments
- Containment experiments
- Simple containment analysis.

These investigations are described here. The main results are presented in Sections III, IV, and V.

A.   Dynamic SLG Extrusion Experiments

Part of the DNA SAC program is the development and application of advanced finite-difference codes to improve calculations on grout flow along a tunnel. A dynamic grout extrusion experiment[5] was developed to provide results for code validation.

Figures 1 and 2 show the extrusion apparatus in which a cylindrical specimen of superlean grout (SLG) in a steel container is driven into a concentric tunnel in a Lucite cylinder by a steel piston. The energy source is a charge of low pressure explosive consisting of an 80/20 mixture by weight of PETN powder and plastic microballoons. The gaseous detonation products pass through holes in two baffle plates to fill an expansion chamber. The resulting pressure acts on a diaphragm and is transmitted to the piston through a layer of oil. With this loading assembly design, innumerable pulse shapes can be obtained having a fairly smooth rise and a very smooth decay.

Instrumentation consists of a high-speed camera that records the SLG surface displacement along the tunnel in the Lucite. This camera also records the piston displacement by observing piston extension rods that move along fixed scales in the camera view. Figure 3 shows typical frames taken from the high-speed camera film of a development test. Two pressure transducers record the pressure in the oil that transmits the

13

explosive gas pressure to the piston. Small colored ceramic beads were cast in the grout for pretest and posttest displacement assessment to supplement the instrumentation data.

The SLG, designated HSSL-1A because it is made with the formula for HSSL-1, is a grout with well characterized material properties[2] (Figure 4); 14-day aging was selected.

Figures 5 and 6 show the two SLG containers used in the experiments. These containers serve as molds for SLG pouring and aging and as nozzles for the extrusion process.

In typical experiments, 35 grams of explosive mixture produced piston pulses with maximum pressures of 600 to 900 psi, times to reach maximum pressures from 4 to 6 msec, and durations greater than 14 msec. Grout surface displacements in 1-1/2-inch-diameter tunnels ranged from 3 inches in 11 msec to 4 inches in 13 msec. Maximum surface velocities ranged from 25 to 45 feet/sec. Results are presented in Section III.

An unknown in the extrusion experiments is the shear stress at the steel boundary of the grout caused by friction between the grout and steel or, in the case of no relative interface motion, local shear stress flow. To provide friction data, an experiment was devised that consists of measuring the resistance of a SLG piston to motion along a steel cylinder. Figure 7 shows the SLG piston held between two short steel pistons that are connected to each other by a central steel rod. Before this composite piston is projected along the steel cylinder, the SLG is subjected to pressure by rotating one steel piston on the threaded rod. The pressure is calculated from circumferential strain gage or diameter change readings along the cylinder. The composite piston is attached to the piston of the extrusion apparatus of Figures 1 and 2 after removing the extrusion portion of the assembly. The pressure applied to the piston and the resulting motion are recorded and the friction force determined from the simple equation of motion.

14

B.   Containment Experiments

A laboratory experiment[6] was devised and developed to investigate the effect of a residual stress field on containment. The first objective of this experiment is to demonstrate that a residual stress field exists around an exploded cavity. The second objective is to establish the extent to which the residual stress field aids containment. The experiment is shown schematically in Figure 8. A small spherical explosive charge representing the nuclear device is sealed and cast in a much larger sphere of grout with properties similar to those of Nevada Test Site tuff (Figure 8a). The grout surface is sealed and hydraulically pressurized to represent overburden (Figure 8b). The explosive is detonated and the residual gases are released (Figure 8c). Fluid is pumped into the cavity at a constant flow rate until fracture causes equalization of internal and external pressures (Figure 8d).

The final stages of gas release and cavity pressurization are included to determine the effect of the residual stress field by comparing the cavity pressure required to crack the RMG sphere with and without residual stresses. In the experiments without a residual stress field, spherical cavities are cast in the grout spheres; the cavities are the same size as the exploded cavities.

Figure 9 shows a 12-inch-diameter RMG sphere inside a steel vessel containing water under pressure. The sphere is suspended from the lid by a threaded steel tube cast in the grout; the tube is used also to position the charge, to guide the detonator cables, and to drill into the cavity after detonation. The water pressure in the vessel was maintained constant (1000 psi) throughout the test series by incorporating a high-pressure gas reservoir and valve in the water supply line.

Figure 10 shows the constant flow rate system. The specifications are listed in Table 1. The motor shaft rotates at a constant angular velocity (6 rpm). A slotted tubular coupling allows an extension of the shaft to translate as well as to rotate. The shaft extension is threaded and rotates in a fixed threaded bearing causing constant velocity translation of the pump piston. Hence, fluid is driven at a constant rate into

15

the cavity supply line (Figure 9). Fluid flow is recorded automatically with pen and chart by measuring the voltage change across an angular potentiometer geared to the rotating shaft; chart speed introduces time, and calibration test results relate voltage change to flow (11.2 cm^3/volt). Similarly, pressure is recorded by measuring the voltage change across a calibrated electrical resistance pressure transducer.

Figure 11 shows the explosive charge used in all but two early tests. It contains 1 gram of PETN. The charge has to be carefully sealed against water in the surrounding grout being squeezed between the spherical container and the bridge plug to soak the PETN and prevent detonation. In future charge designs, the amount of inert material, especially the bridge plug, should be reduced to improve spherical symmetry.[9]

Figures 12 and 13 show properties of the rock matching grout used in the experiments.

C. Simple Containment Analysis

A simple containment analysis[7] was performed to aid in understanding the mechanics of dynamic cavity expansion and to supplement similar work that has been done by computer codes. In the formulation, a gas with a known equation of state is assumed to instantaneously pressurize a spherical cavity in a solid homogeneous and isotropic medium. A simple analytical treatment of the subsequent cavity expansion was made possible by idealization of the following material properties:

- Incompressibility
- Elastic-perfectly plastic behavior
- Yielding according to the Mises condition
- Plastic straining according to the associated flow rule.

Overburden is included as a constant pressure infinitely far from the cavity.

The gas pressure causes cavity expansion and creates a distribution of outward radial particle velocity in the medium. As expansion proceeds, the gas pressure decays and the tensile tangential stresses increase to

16

slow down expansion and eventually cause rebound of the medium. Subsequent, relatively small amplitude oscillations occur until the kinetic energy is dissipated; in the analysis, the energy dissipates only by plastic work of distortion. During expansion and contraction, plastic zones spread out from the cavity and greatly influence the character of the stress fields. The highly compressive character of the residual stress field takes shape during the rebound.

The analysis is presented in SRI Topical Report 3702-2 (Reference 7). Conclusions based on the analysis are given in Section V.

Table 1

HYDROFRACTURE SYSTEM SPECIFICATIONS

Motor: Dayton Gear motor model 5K933
        1/4 HP, 6 rpm, 600 in-lb torque

Pump: High Pressure Equipment Co. Model 87-6-5
       60 cm^3 capacity, 5000 psi maximum pressure
       4.26 cm^3/min. flow rate (0.71 cm^3/revolution)

System: Fluid: Dyed Glycerin
        Volume (excluding pump) 31.33 cm^3.
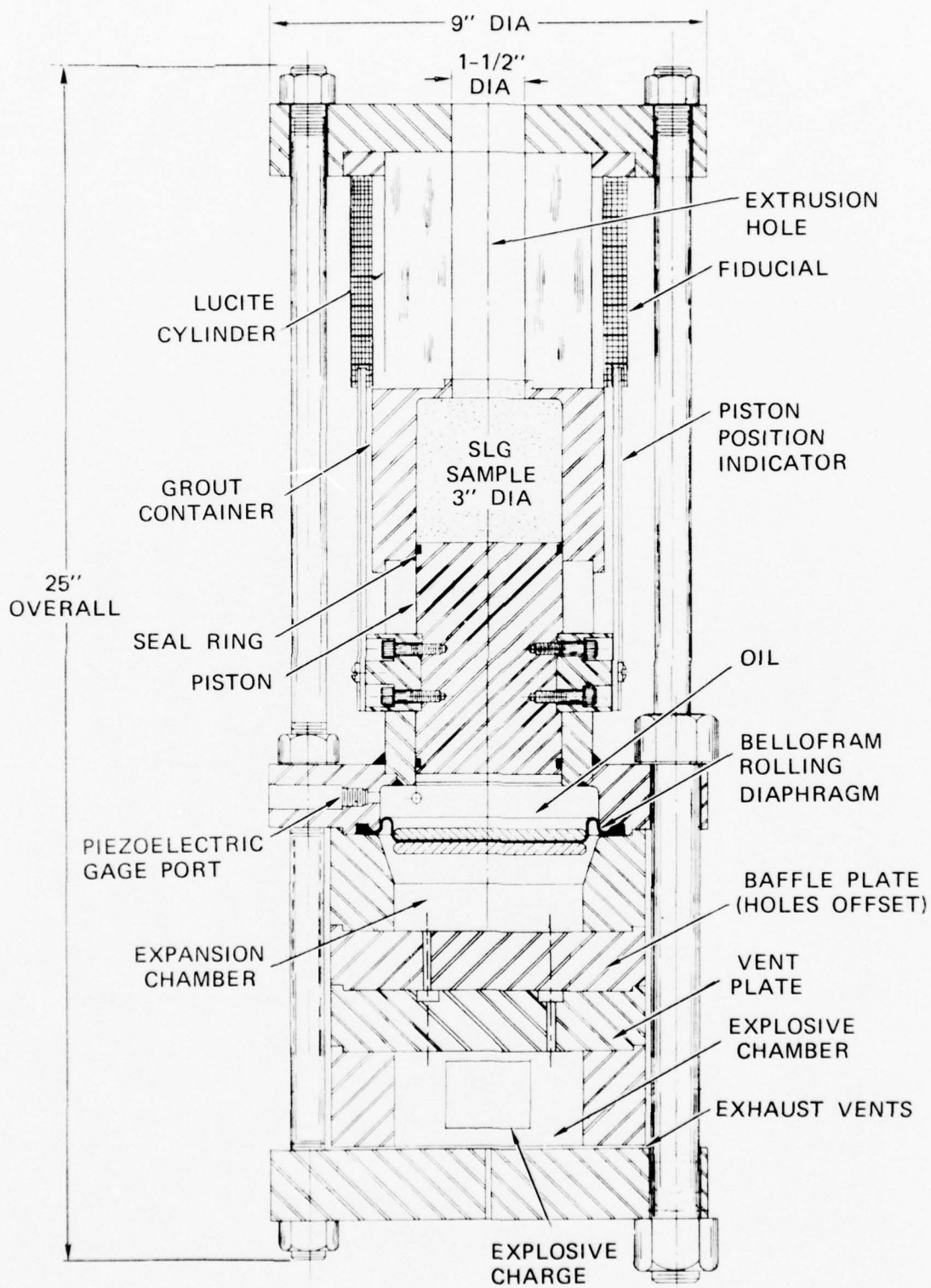
FIGURE 1   PISTON-DRIVEN EXTRUSION APPARATUS

MA-3702-14B

19
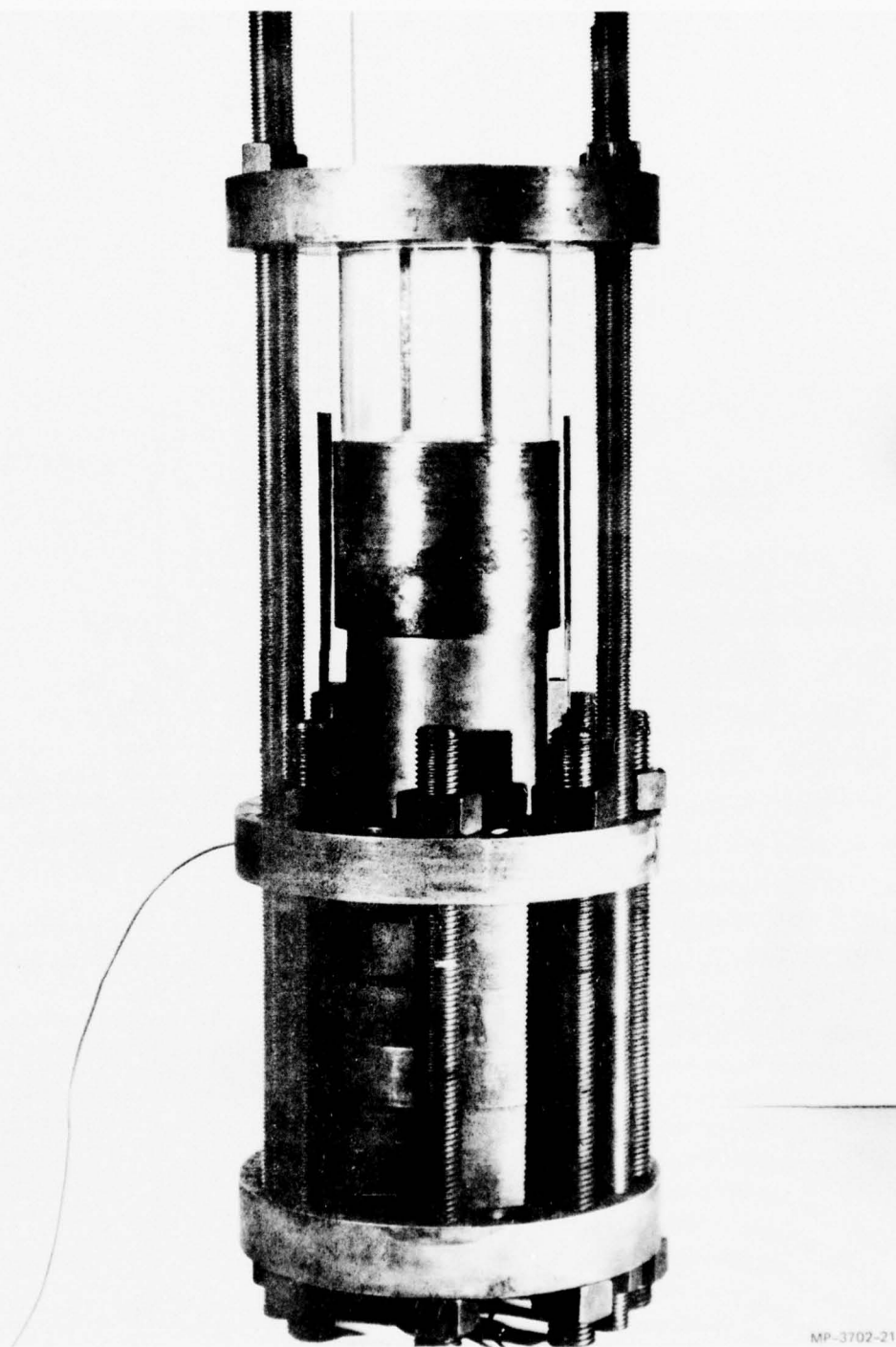
FIGURE 2   PHOTOGRAPH OF AXIALLY DRIVEN SLG EXTRUSION APPARATUS

MP-3702-21

20

T = 0

4.020 msec

1.005 msec

5.025 msec

2.010 msec

6.030 msec

3.015 msec

7.035 msec
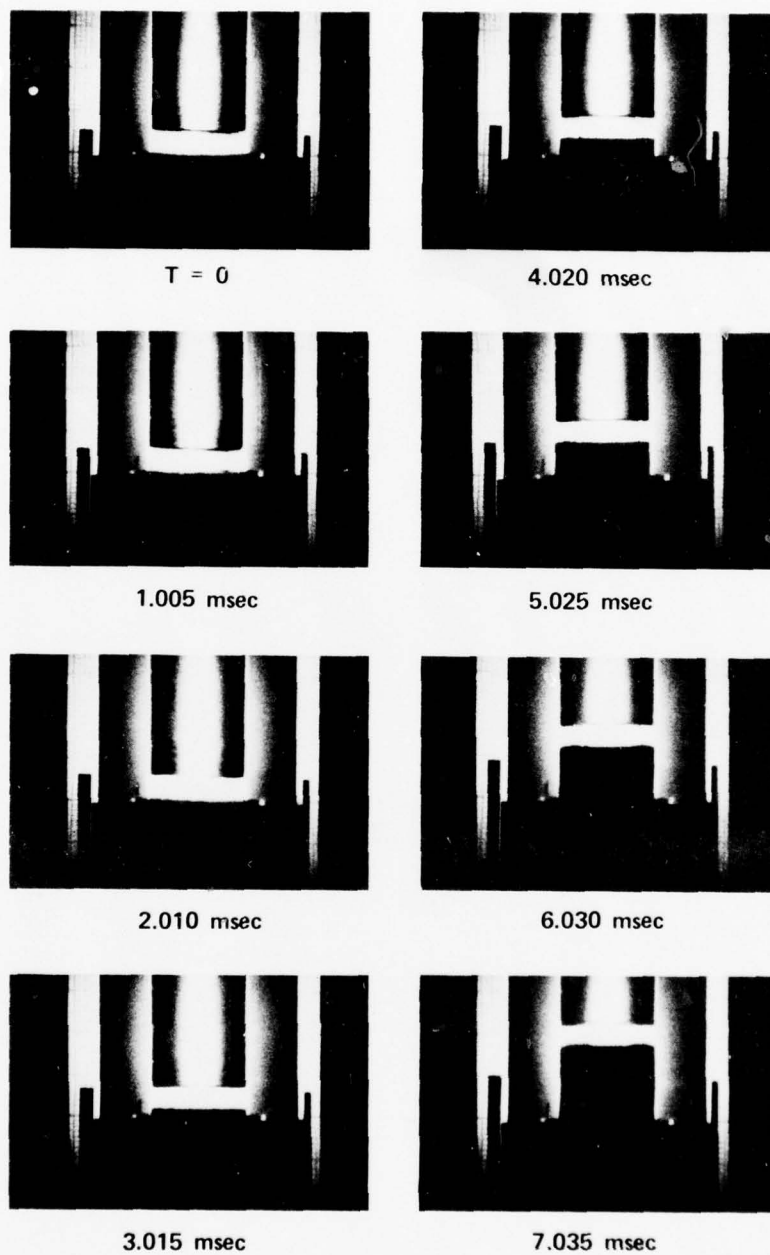
MP-3702-43

FIGURE 3   DYNAMIC EXTRUSION OF AXIALLY DRIVEN SLG (TEST 102)
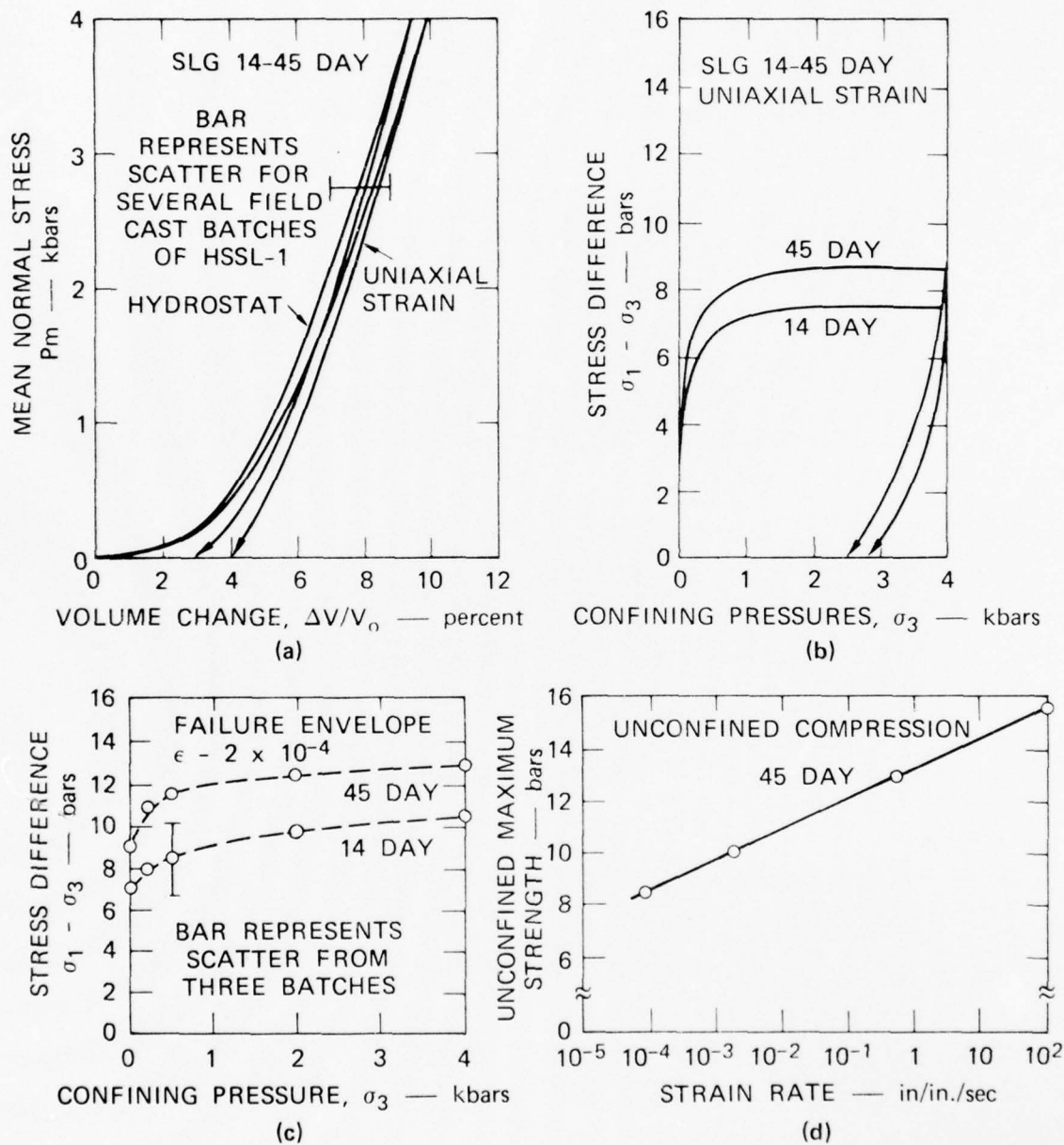
FIGURE 4   PROPERTIES OF HSSL-1
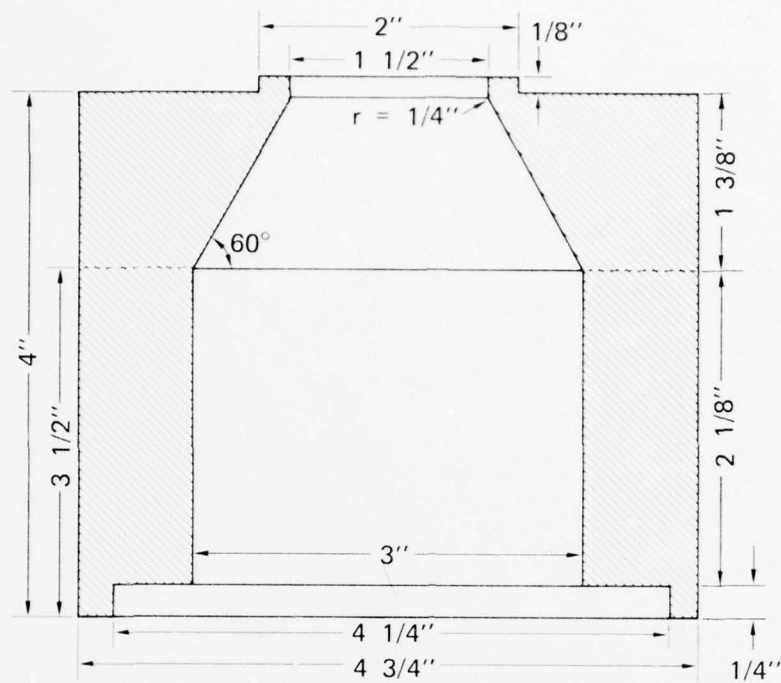
MA-3702-13

MA-3702-117

FIGURE 5   CONICAL-CYLINDRICAL MOLD FOR SLG SPECIMEN
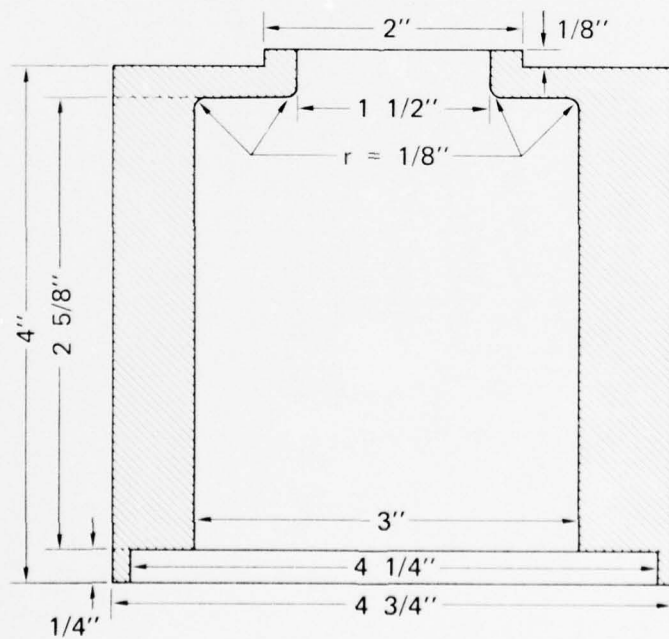
MA-3702-116

FIGURE 6   CYLINDRICAL MOLD FOR SLG SPECIMEN

23

3" ID

2"

HEXAGONAL BOSS

1"

STEEL PISTON

1/8-INCH THICK
STEEL TUBE

3/4"

8"

SLG

STUD

STEEL PISTON

O-ring (1/8" OD)

1"

1/2"

3/8"

3/8"

1 1/2"

Piston (Figure 1)

3 1/4" OD
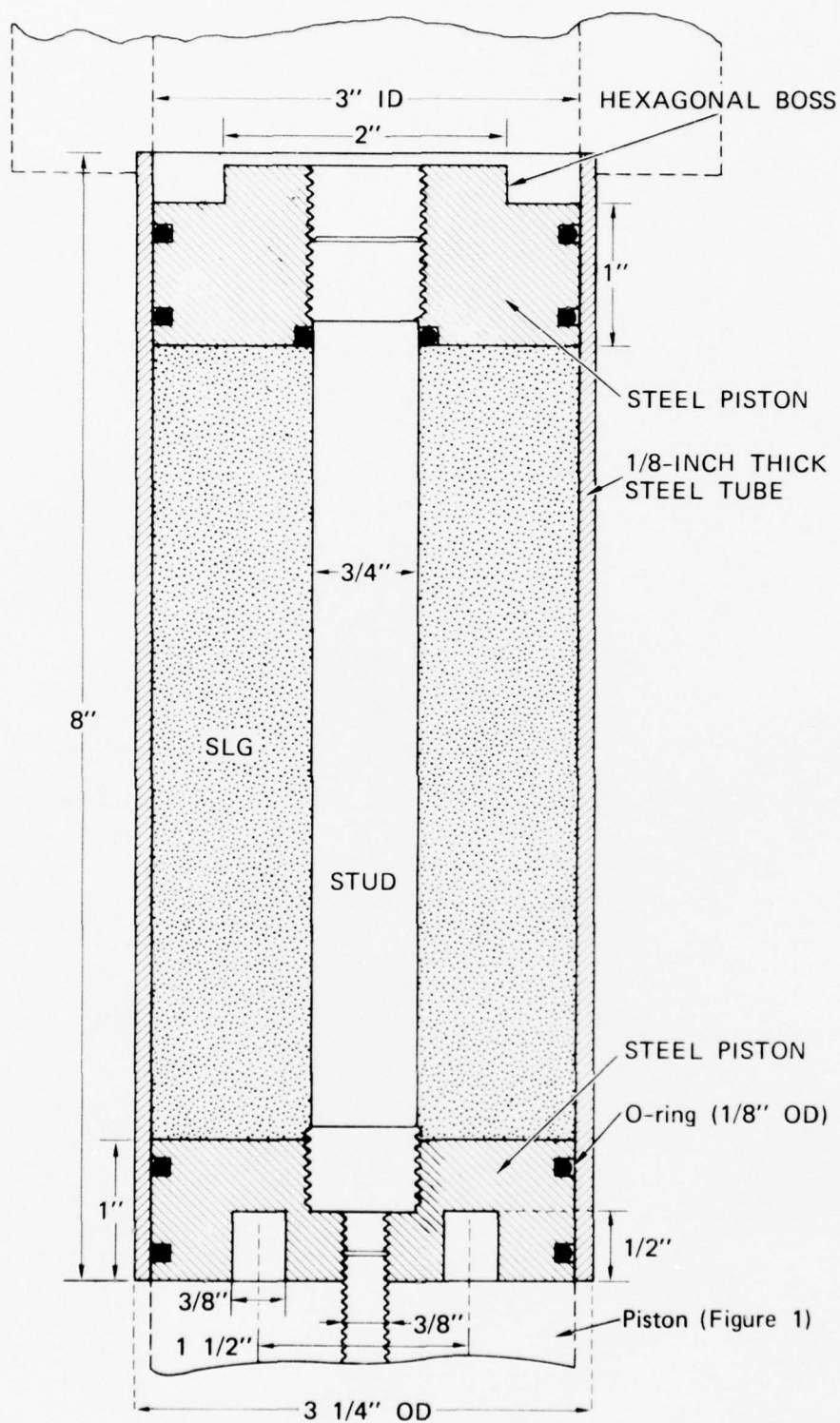
MA-3702-118

FIGURE 7   COMPOSITE PISTON FOR DYNAMIC FRICTION MEASUREMENTS

24
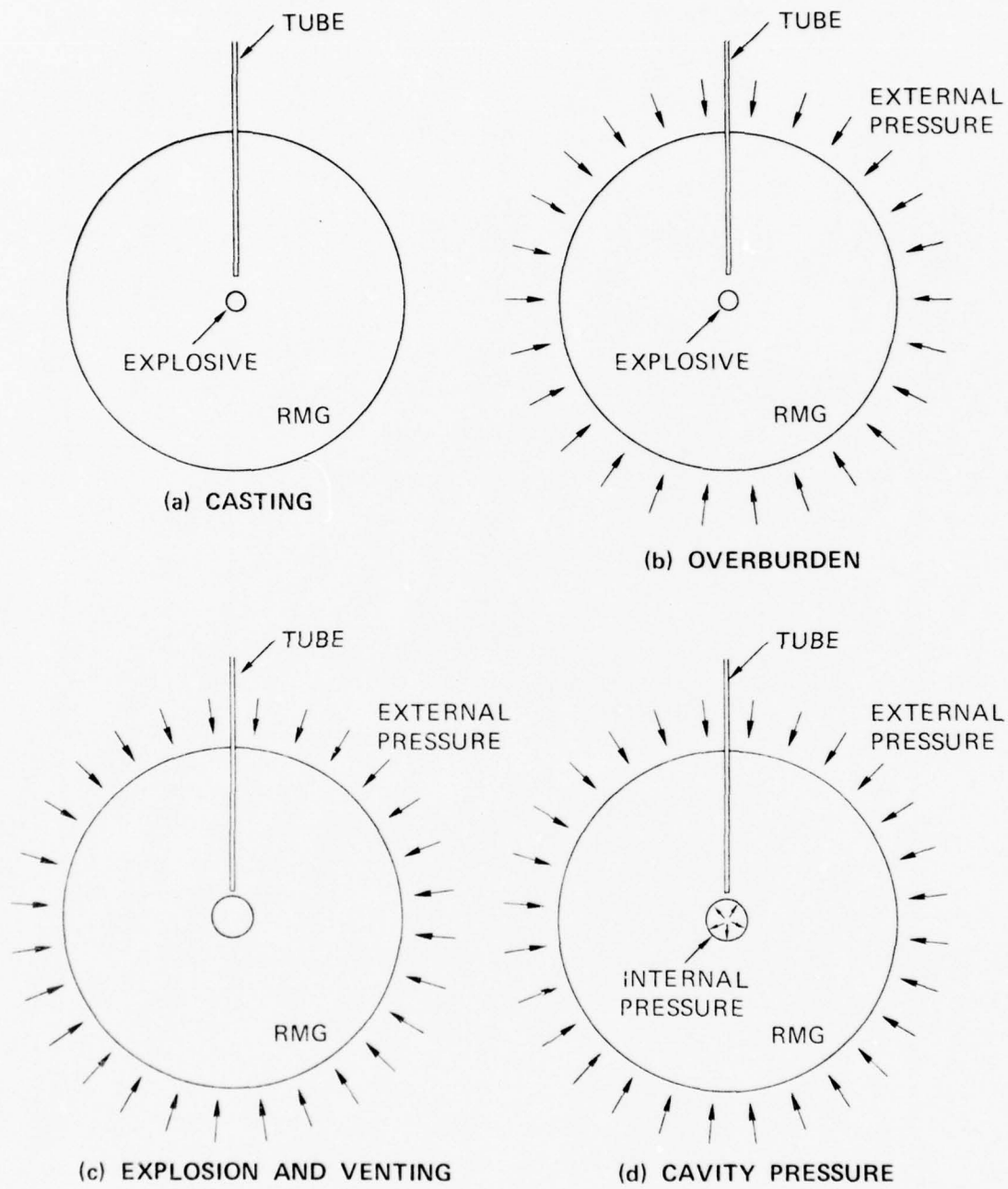
FIGURE 8   SEQUENCE OF OPERATIONS IN CONTAINMENT EXPERIMENT
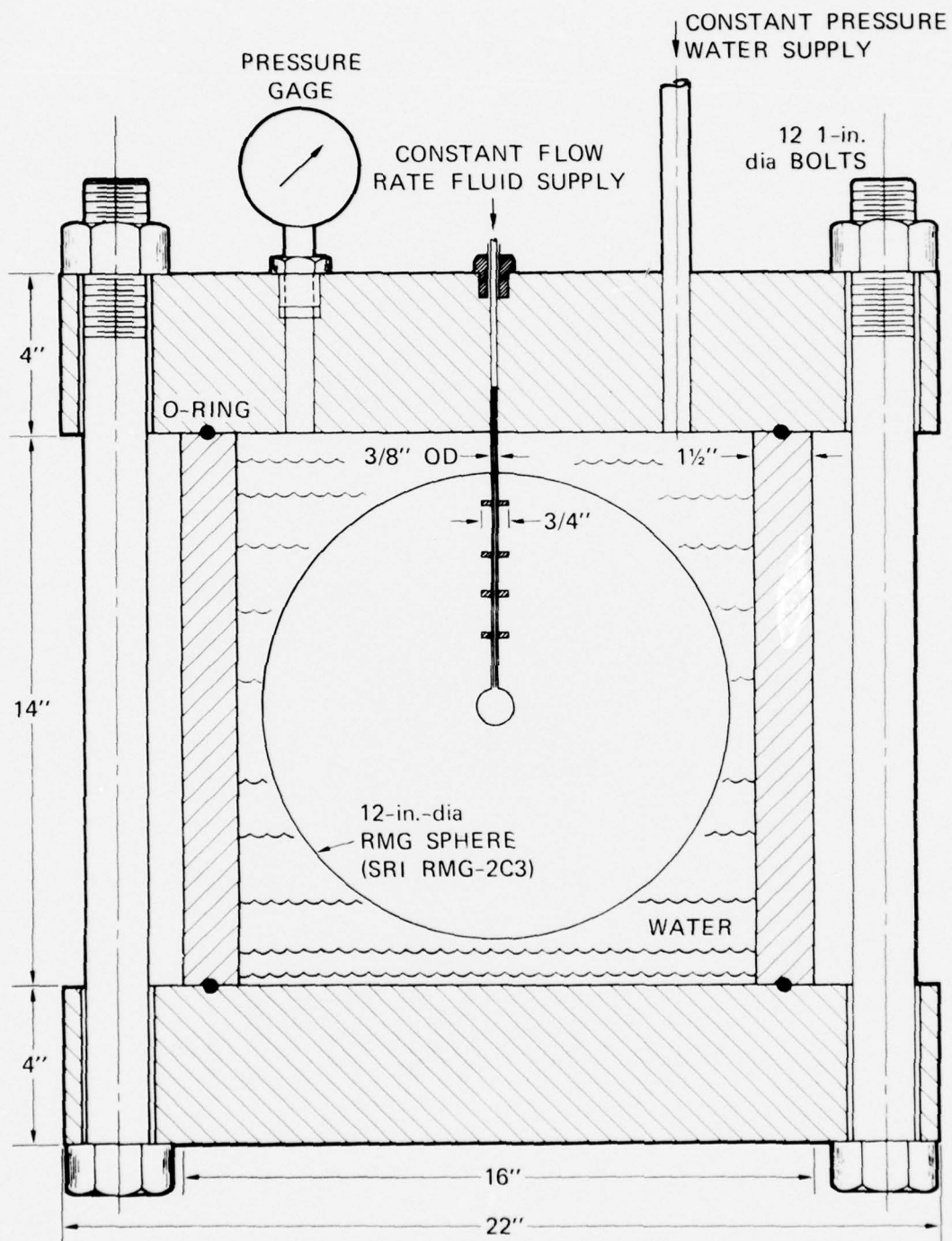
25

FIGURE 9   CONTAINMENT EXPERIMENT APPARATUS

MA-3702-105

GEAR MOTOR
HP 0.25
RPM 6

5³⁄₄"

9"

GEAR WHEELS

SUPPORT BRACKET

GEAR WHEELS

3"

16/8"

1"

4"

½"

3"

COUPLING

7¼"

POTENTIOMETER

1½"

6¼"

9½"

HYDRAULIC FLUID

PISTON

HIP PUMP
5000 psi max
60 cm³ capacity

2¼"
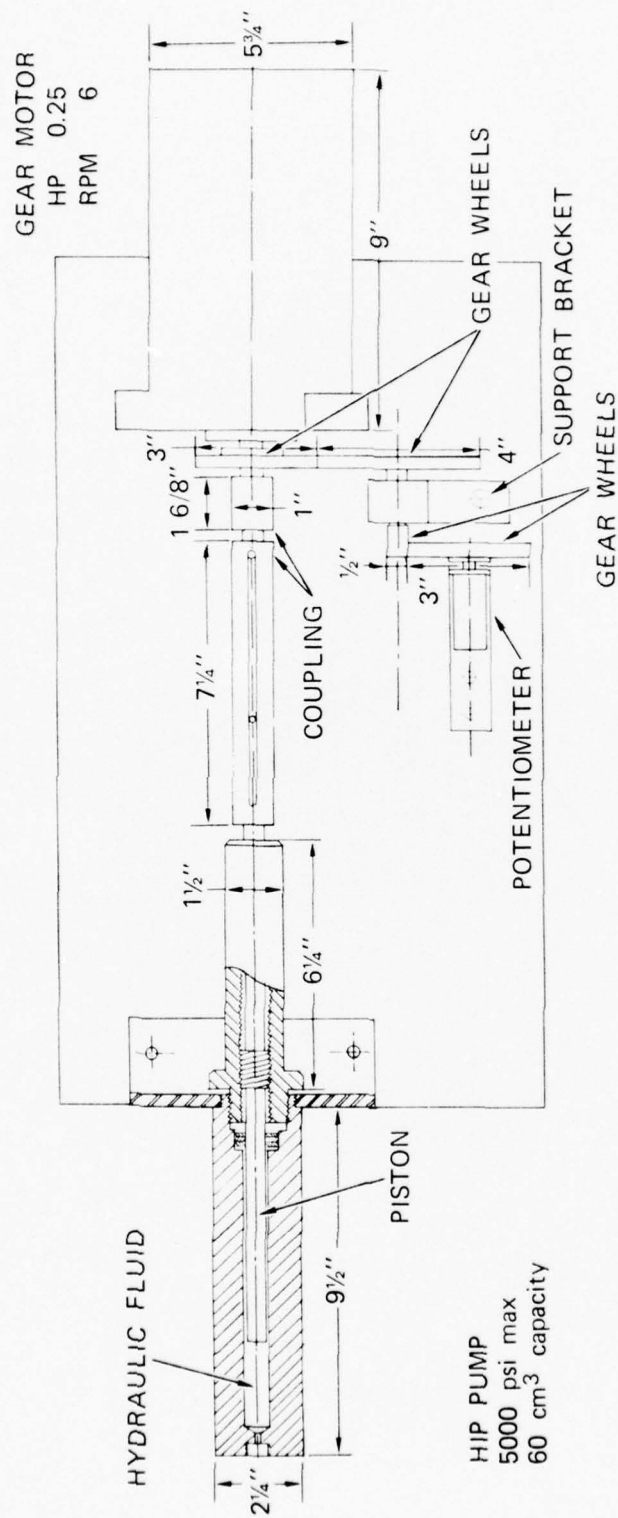
MA-3702-107

FIGURE 10   CONSTANT FLOW-RATE HYDROFRACTURE SYSTEM

27
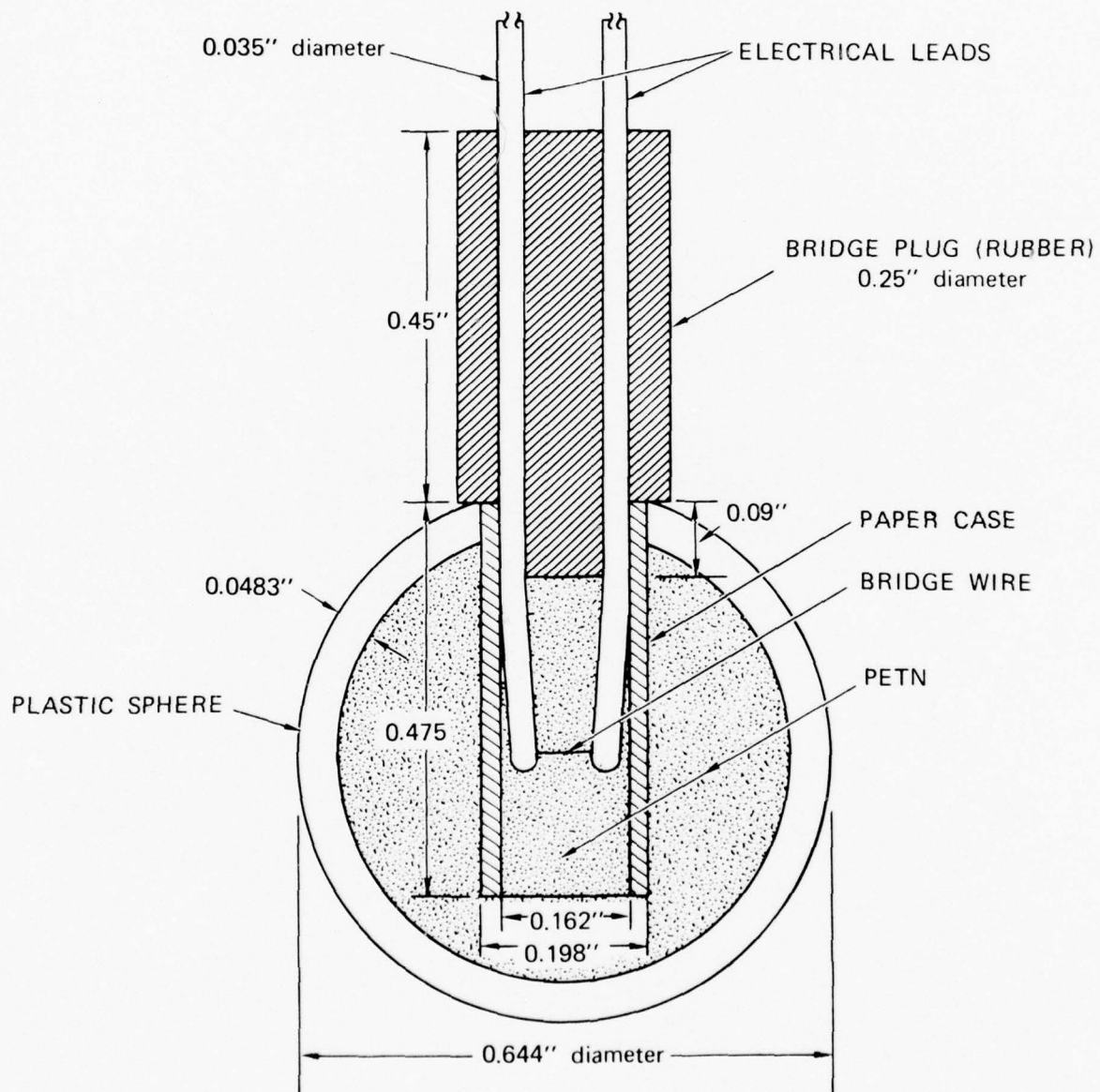
FIGURE 11   EXPLOSIVE CHARGE DETAILS

MA-3702-108

28
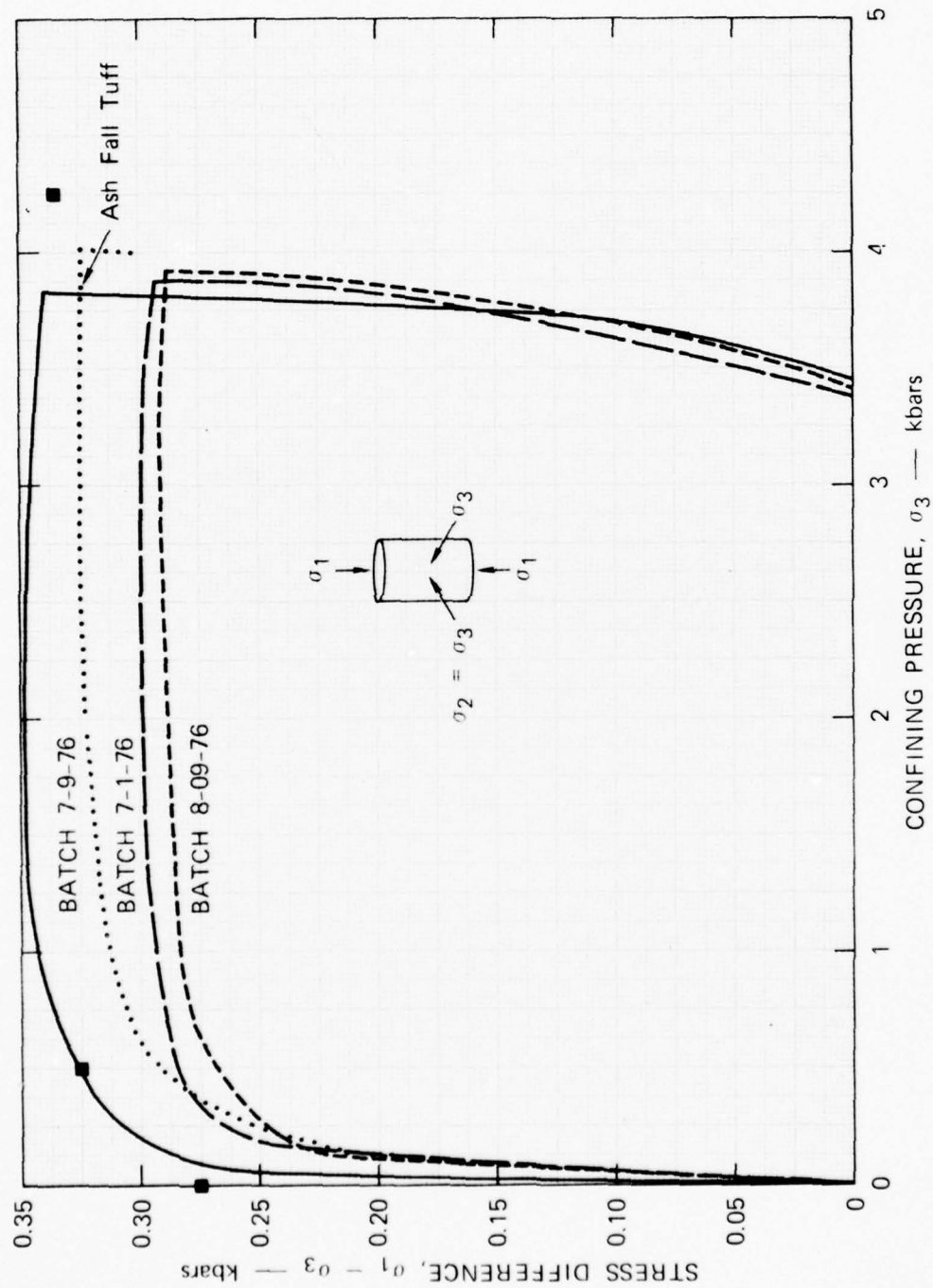
FIGURE 12   STRENGTH PROPERTIES OF THE ROCK-MATCHING GROUT SRIRMG-2C3
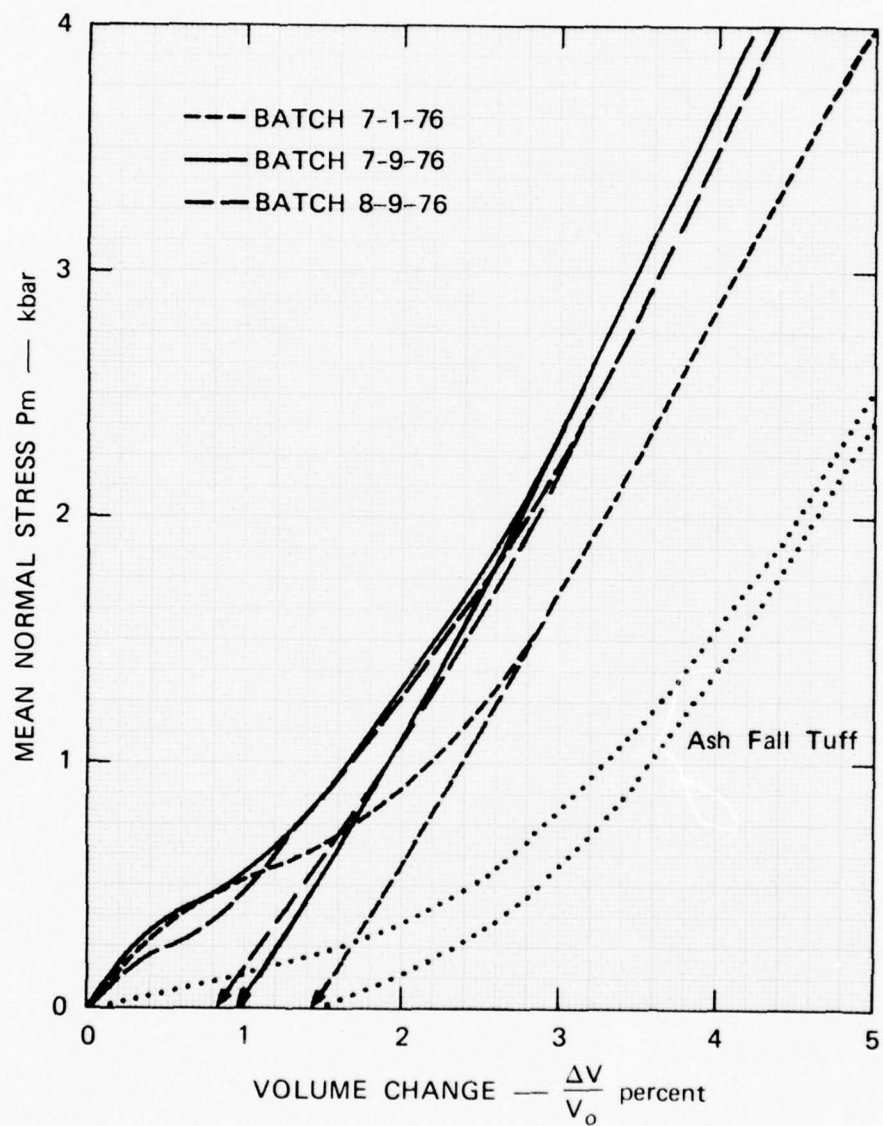
MP-3702-119

FIGURE 13   STRENGTH PROPERTIES OF THE ROCK-MATCHING GROUT SRI RMG-2C3

MP-3702-120

30

III   EXTRUSION EXPERIMENTAL RESULTS

A.   Extrusion Experiments

Table 2 shows the organization of the data for six dynamic extrusion tests arranged in three groups of two tests. Groups 1 and 2 have the same cone-cylinder configuration (Figure 5), different piston pressures (Figure 14), and grout from different batches (Table 5). Group 3 has the cylindrical configuration (Figure 6), piston pressures comparable to those of Group 2 (Figure 14), and grout from the same batch as Group 2 (Table 5).

Figures 14 and 15 show the group average piston pressures and impulses, and Figure 16 and 17 show the group average SLG front and piston displacements. Two transducers monitored the pressure in each test. The two pressure records were averaged to provide the test average pressure. In each group, the two test average pressures were averaged to provide the group average pressure.

Figures 18 to 29 present the results by groups to allow a comparison of the two test results in each group. The pressures and impulses being compared are test averages.

Tables 3 and 4 give the initial and final locations of particles (colored ceramic beads) cast in the grout. Figures 30 and 31 explain the XY coordinate system and show diagrams of the particle locations and sample shapes.

B.   Friction Experiments

Tests 111 and 121 were performed to obtain the friction between the SLG and the steel container. In both tests, the SLG in the steel tube (Figure 7) was squeezed between the two steel end plates to a pressure of 1000 psi. Figures 32 and 33 show the pressure pulses applied to the

31

piston in Tests 111 and 121, and Figures 34 and 35 show the resulting piston displacements.

The equation of piston motion is

$$pA = M\frac{d^2x}{dt^2} + fS \qquad (1)$$

where

p = pressure applied to the piston (Figures 32 and 33)
A = piston area (45.6 cm^3)
M = piston mass (7808 grams)
x = piston displacement (Figures 34 and 35)
f = friction
S = surface area between steel and SLG (361.3 cm^3)

The friction results of Figure 36 were determined by using a fifth degree polynomial for a least squares fit of the x-t data to determine the piston acceleration in Equation (1). Approximate averages are 2-1/2 and 3 bars (36 and 43 psi); a fourth degree polynomial gave the same results. A useful addition to the experiment would be an accelerometer attached to the piston to attempt to measure directly the acceleration required in Equation (1).

C.   Properties of SLG

Table 5 gives SLG properties obtained from batch samples. Results for Tests 158 and 159 are included because the samples experienced negligible extrusion under Group 2 loading and sample configuration (same as Tests 140 and 141). The slightly higher crush strength implies proximity to the threshold of extrusion. Figures 37 and 38 show strength properties determined by Terra Tek from samples of the grout batch for Tests 158 and 159.

The main improvement required in the extrusion experiment is a reduction in scatter of the SLG properties. Table 5 shows that for the HSSL-1A mixture of Table 6, unconfined crush strengths can vary from 124 to 174 psi

32

even with precise weighings with dried fines, same mixing times, careful sealing, and same aging periods and temperatures. Because of the small batches required for the samples, a sieve analysis was conducted on six samples of the Nevada Test Site fines. The results are listed in Table 7 and are indicated by the bars in Figure 39. Three particle size distributions were prepared, according to Table 8 and the points in Figure 39, and used in the HSSL-1A mixture of Table 6. After 14 day aging, the samples were subjected to unconfined crush tests. Results are given in Table 8. Although the tests are limited in number, the strengths exhibit a trend with reduced scatter. It is recommended that design size distributions be incorporated in future extrusion tests if further strength tests consolidate the findings in Table 8.

Table 2

ORGANIZATION OF SLG EXTRUSION DATA[a]

| Group | Test | SLG Configuration | Figure Number | | | | | Table |
			Piston Press.	Piston Impulse	SLG Displ.	Piston Displ.	Particle Displ.	Particle Displ.
1	134	Cone-cylinder	14,18	15,19	16,20	17,21	30	
	135	(Figure 5)					31	3
2	140	Cone-cylinder	14,22	15,23	16,24	17,25	--	
	141	(Figure 5)					--	3
3	142	Cylinder	14,26	15,27	16,28	17,29	--	
	143	(Figure 6)					--	4

[a]Technical Report TR 76-3702-4 (Reference 5) contains the complete data.

Table 3

PARTICLE LOCATIONS BEFORE AND AFTER EXTRUSION

BEFORE	COORDINATES AFTER EXTRUSION[a]											
X = 0	TEST 134			TEST 135			TEST 140			TEST 141		
X = 0.5	X = 0	X = 0.5 before		X = 0	X = 0.5 before		X = 0	X = 0.5 before		X = 0	X = 0.5 before	
Y	Y	X	Y	Y	X	Y	Y	X	Y	Y	X	Y
3.63[b]	7.43[b]			7.34[b]			7.29[b]			7.20[b]		
3.13	6.93	0.46	6.93	6.84	0.49	6.84	6.79	0.50	6.79	6.70	0.46	6.70
2.63	6.22	0.34	6.14	6.16	0.37	6.05	6.17	0.40	6.04	6.03	0.35	5.92
2.13	4.68	0.25	4.80	4.59	0.23	4.73	4.90	0.29	4.75	4.49	0.23	4.56
1.63	2.67	0.31	2.74	2.66	0.33	2.61	2.78	0.38	2.77	2.49	0.31	2.55
1.13	2.00	0.43	2.02	2.07	0.45	2.02	2.05	0.50	2.02	2.06	0.50	2.08
0[c]	0.90[c]			0.90[c]			0.92[c]			0.93[c]		

[a]Coordinates of embedded ceramic beads

[b]SLG top surface

[c]Piston-SLG interface

35

Table 4

PARTICLE LOCATION BEFORE AND AFTER EXTRUSION

BEFORE X = 0 X = 0.5	COORDINATES AFTER EXTRUSION[a]					
	TEST 142			TEST 143		
	X = 0	X = 0.5 before		X = 0	X = 0.5 before	
Y	Y	X	Y	Y	X	Y
3.56^b				6.20^b		
3.06	6.55	0.50	6.55	5.70	0.50	5.70
2.56				5.11	0.22	5.33
2.06	3.00	0.39	2.92	2.79	0.38	2.96
1.56	2.34		2.32	2.19	0.41	2.23
1.06	1.81	0.50	1.81	1.68	0.44	1.72
0^c	0.82^c			0.67^c		

[a] Coordinates of embedded ceramic beads

[b] SLG top surface

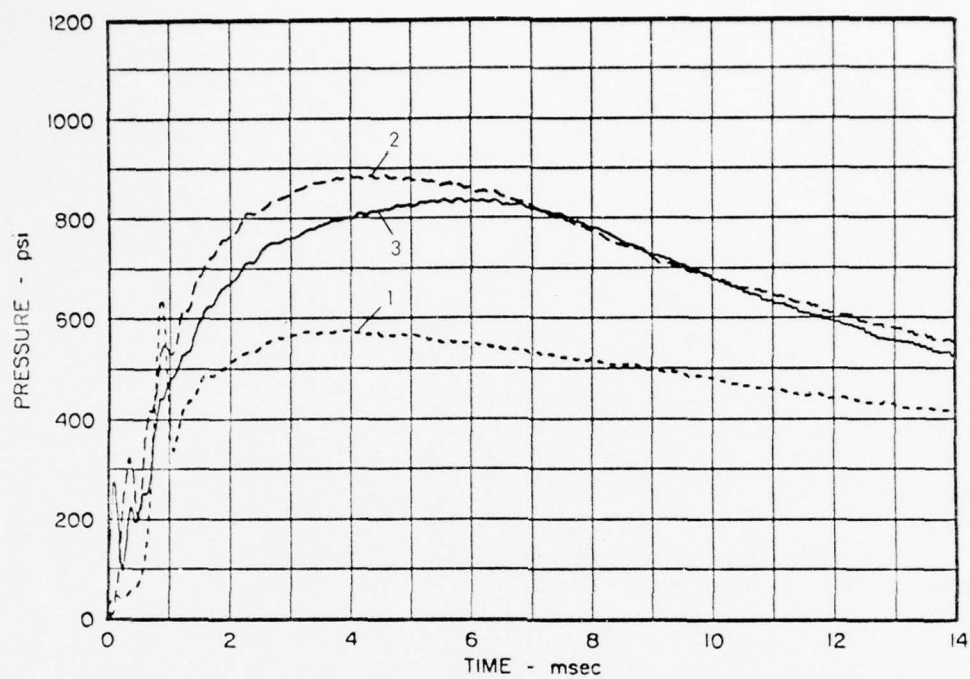[c] Piston-SLG interface

36

FIGURE 14   PRESSURE PULSE AVERAGES FOR TEST GROUPS 1, 2, AND 3
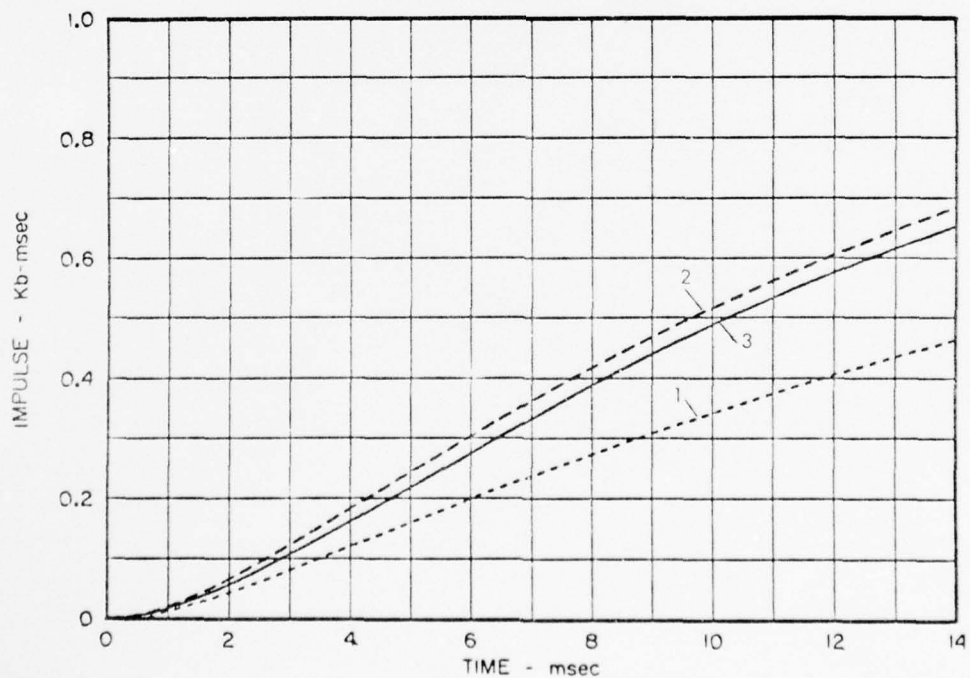
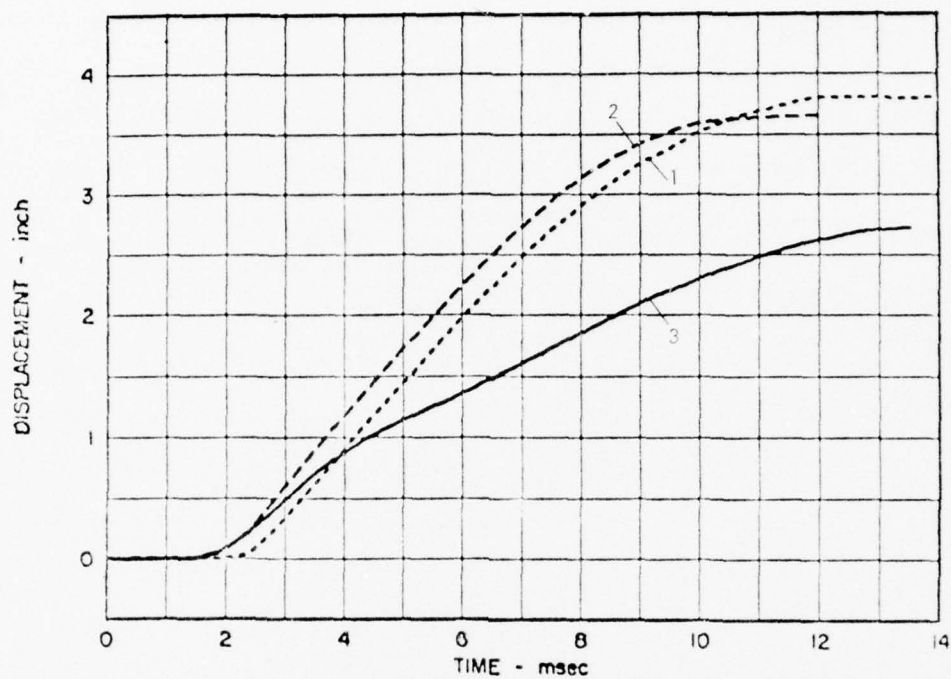FIGURE 15   IMPULSE AVERAGES FOR TEST GROUPS 1, 2, AND 3

37

FIGURE 16   SLG FRONT DISPLACEMENT AVERAGES FOR TEST GROUPS 1, 2, AND 3
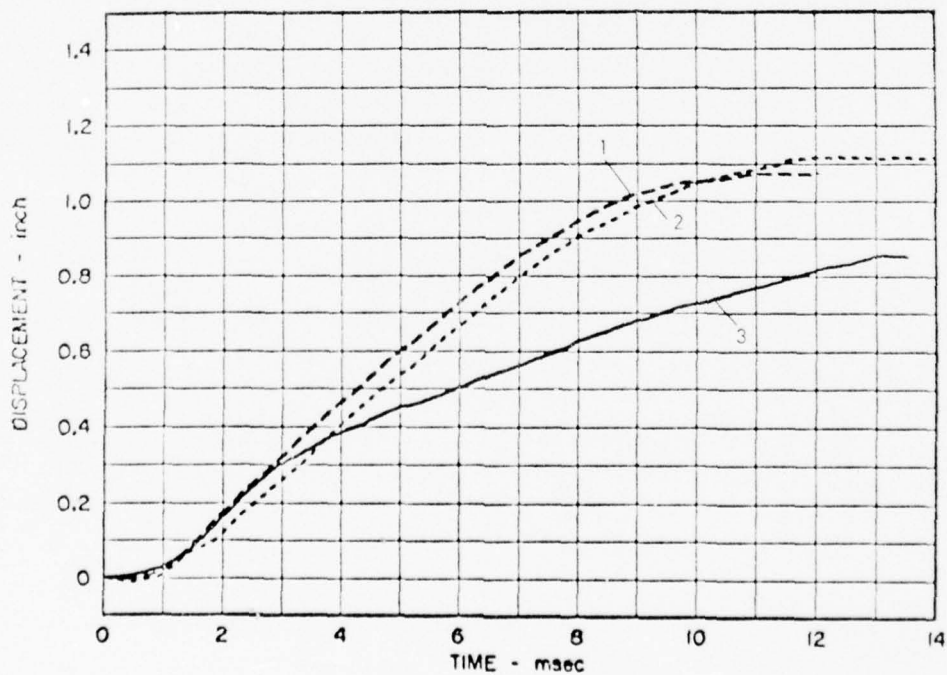

FIGURE 17   PISTON DISPLACEMENT AVERAGES FOR TEST GROUPS 1, 2, AND 3
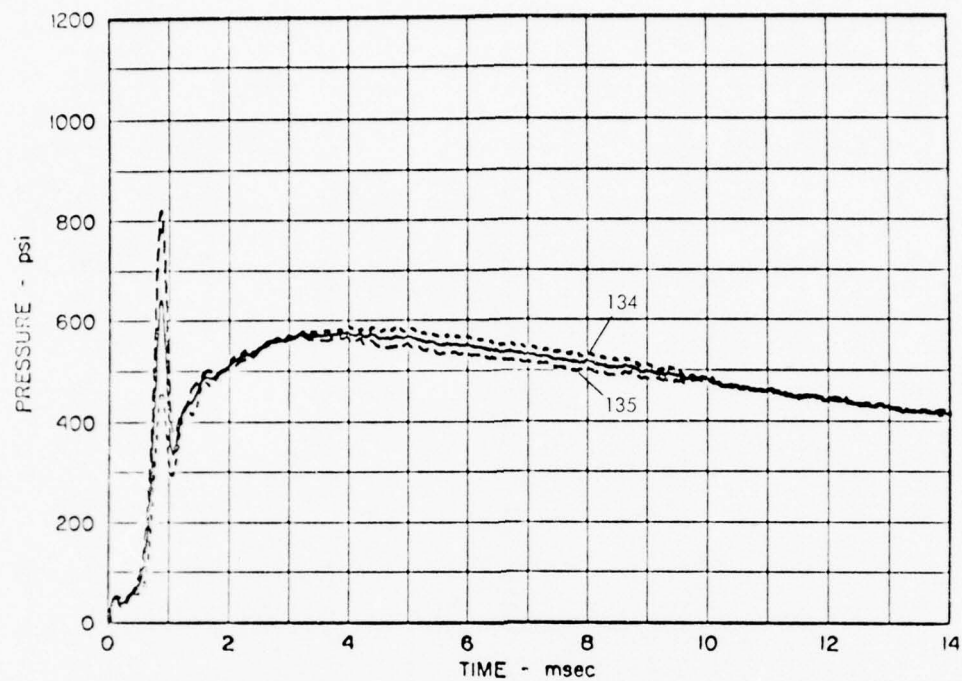
38

FIGURE 18   PRESSURE PULSES FROM GROUP 1 TESTS 134 AND 135
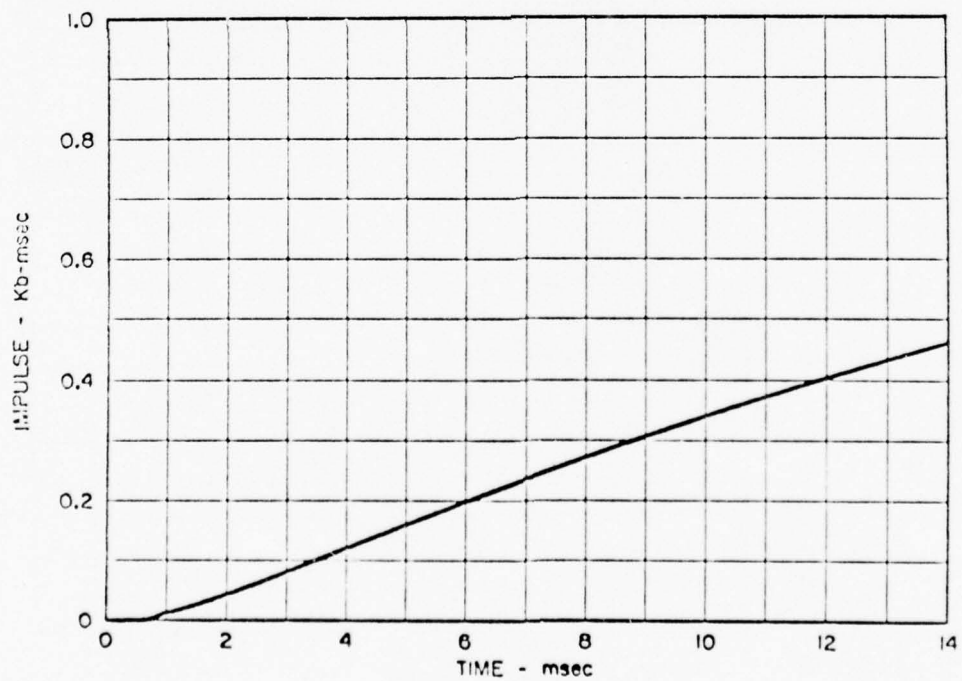

FIGURE 19   IMPULSES FROM GROUP 1 TESTS 134 AND 135

39

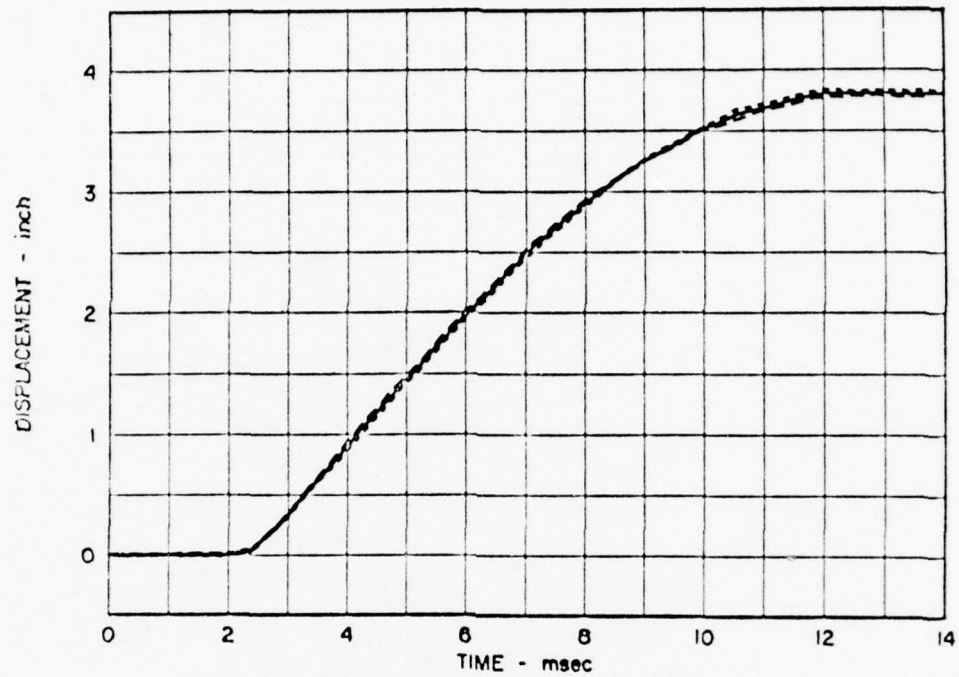FIGURE 20   SLG FRONT DISPLACEMENTS FROM GROUP 1 TESTS 134 AND 135

FIGURE 21   PISTON DISPLACEMENTS FROM GROUP 1 TESTS 134 AND 135

FIGURE 22   PRESSURE PULSES FROM GROUP 2 TESTS 140 AND 141
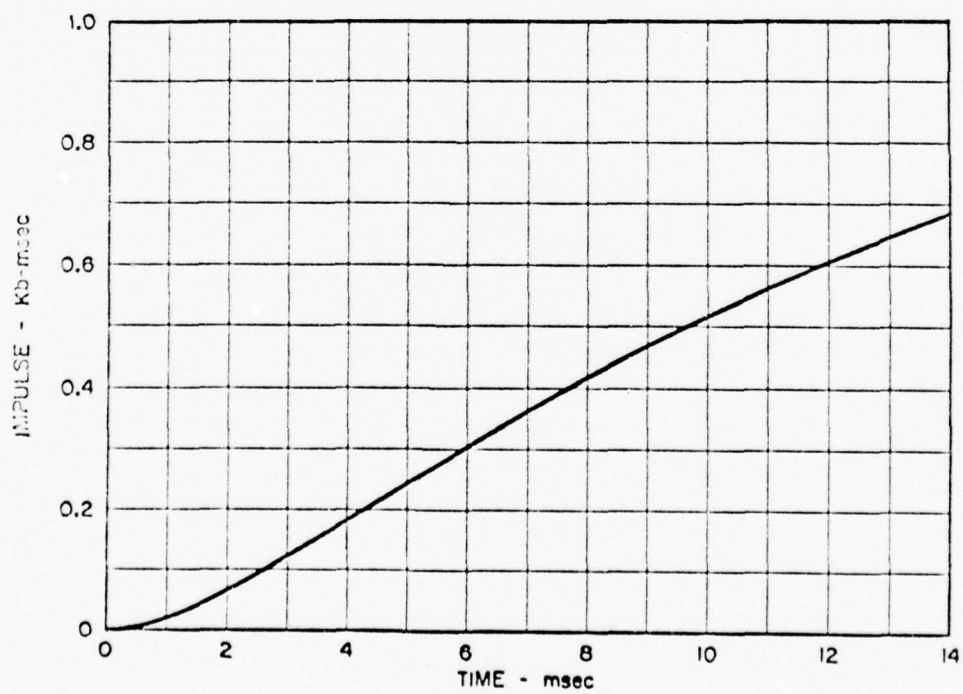
FIGURE 23   IMPULSES FROM GROUP 2 TESTS 140 AND 141

41
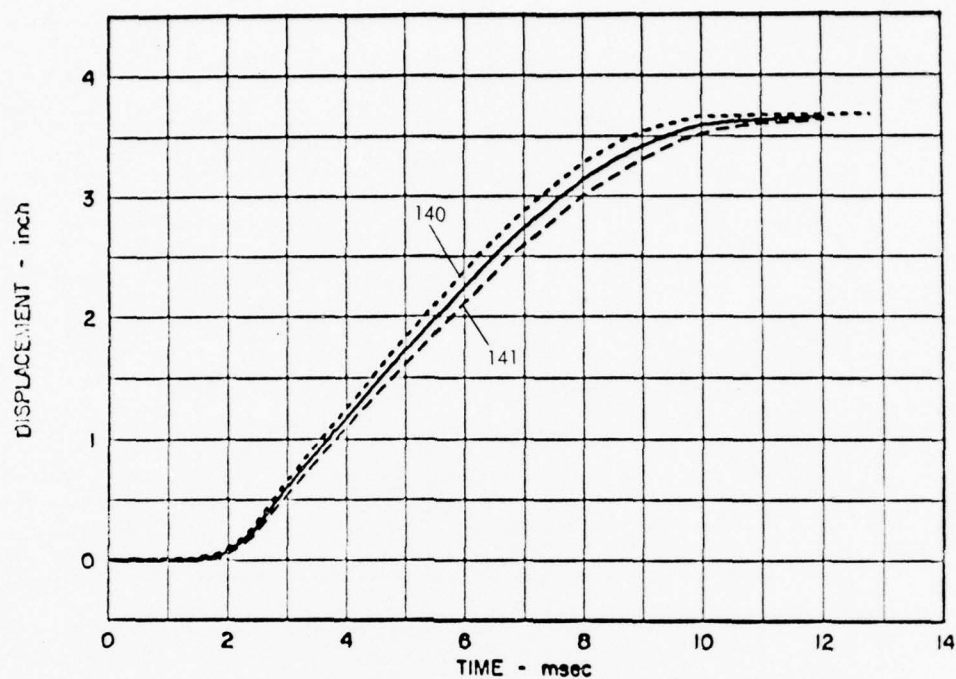
FIGURE 24   SLG FRONT DISPLACEMENTS FROM GROUP 2 TESTS 140 AND 141
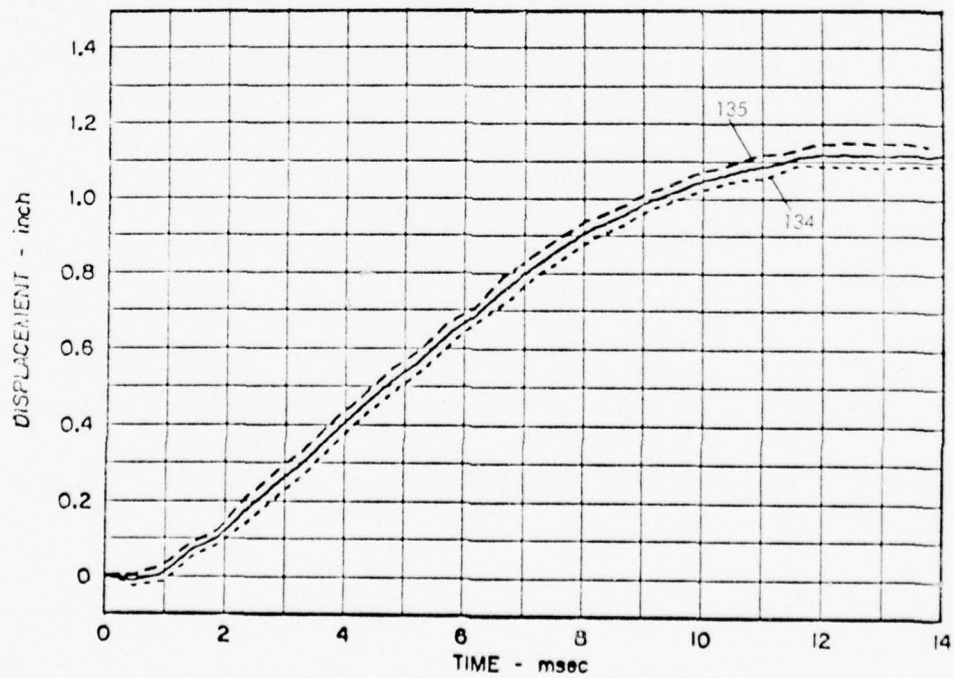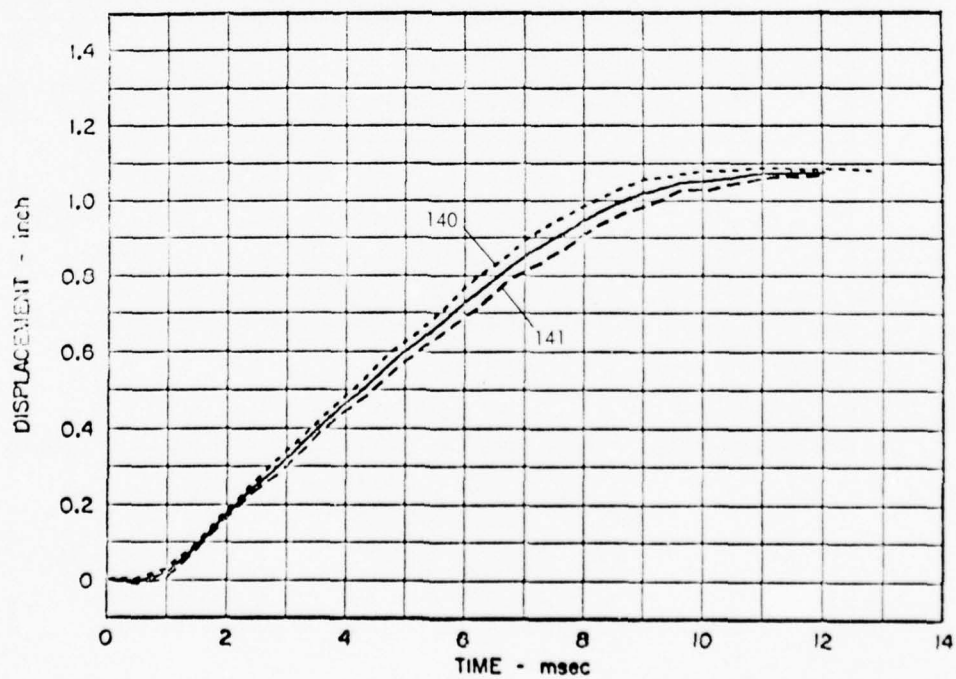

FIGURE 25   PISTON DISPLACEMENTS FROM GROUP 2 TESTS 140 AND 141
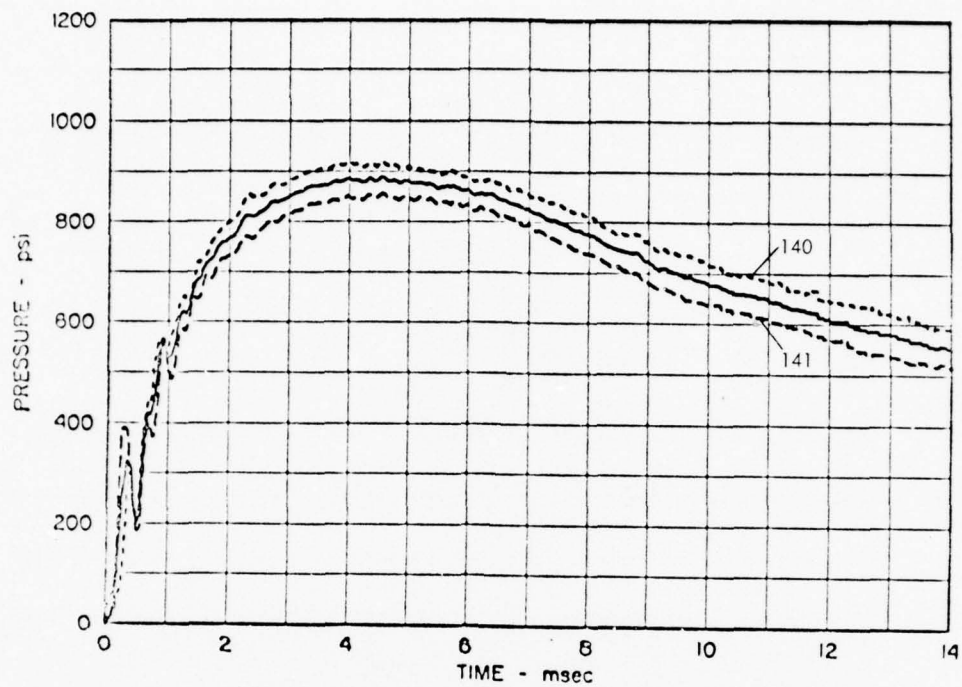
42
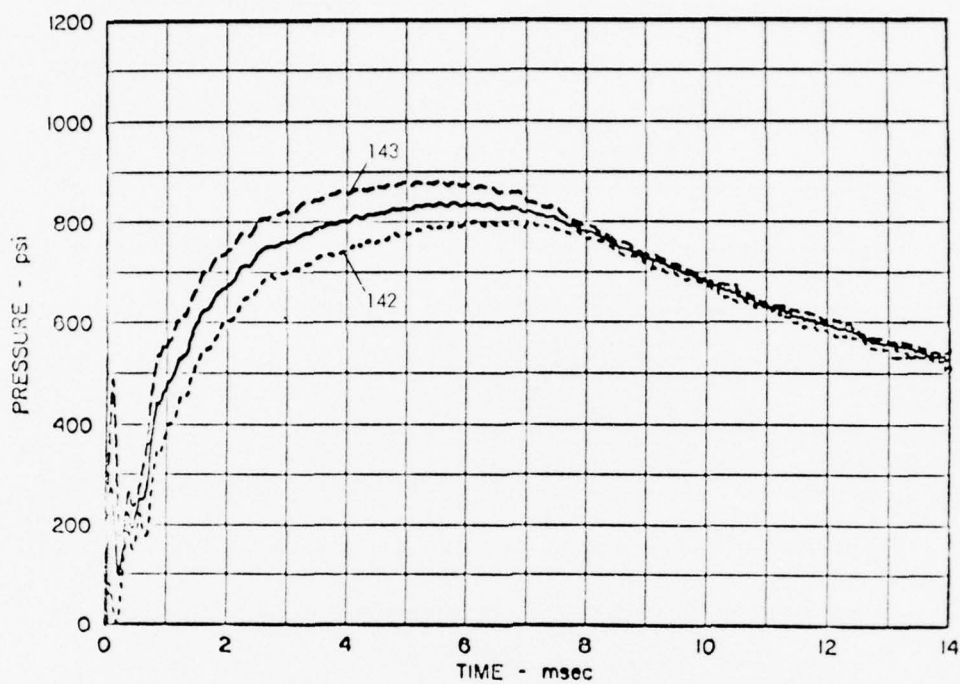
FIGURE 26   PRESSURE PULSES FROM GROUP 3 TESTS 142 AND 143
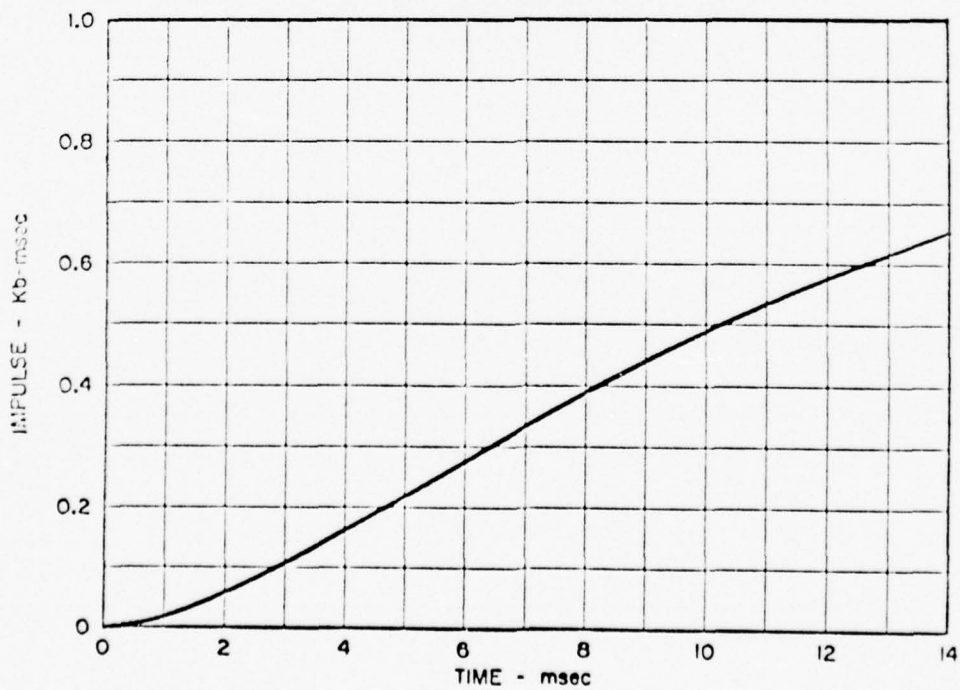
FIGURE 27   IMPULSES FROM GROUP 3 TESTS 142 AND 143

43
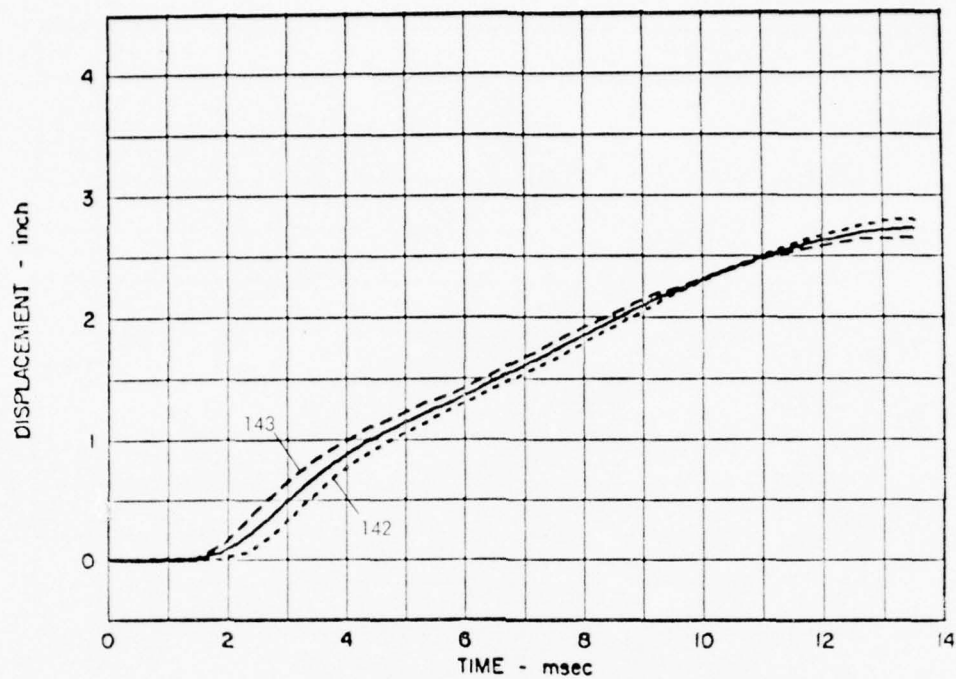
FIGURE 28   SLG FRONT DISPLACEMENTS FROM GROUP 3 TESTS 142 AND 143
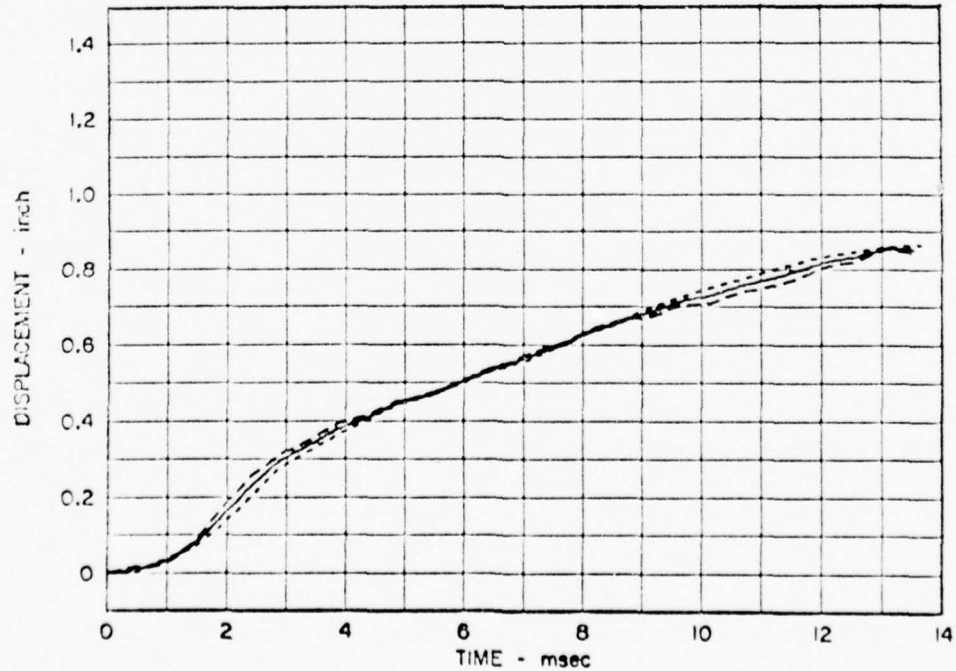
FIGURE 29   PISTON DISPLACEMENTS FROM GROUP 3 TESTS 142 AND 143

44
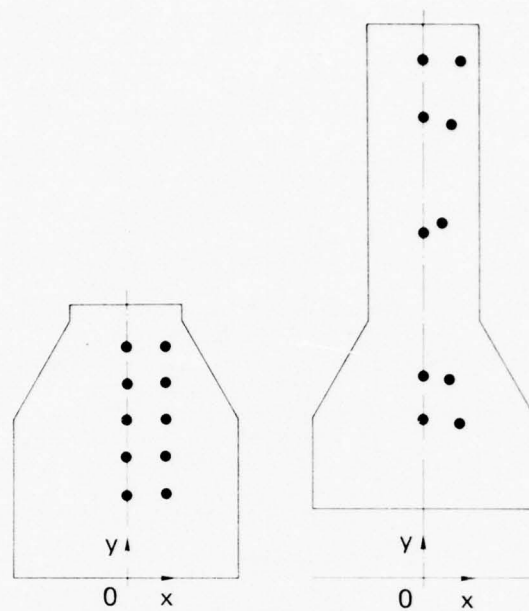
SHOT 134

MA-3702-141

FIGURE 30   INITIAL AND FINAL PARTICLE LOCATIONS FROM
GROUP 1 TEST 134
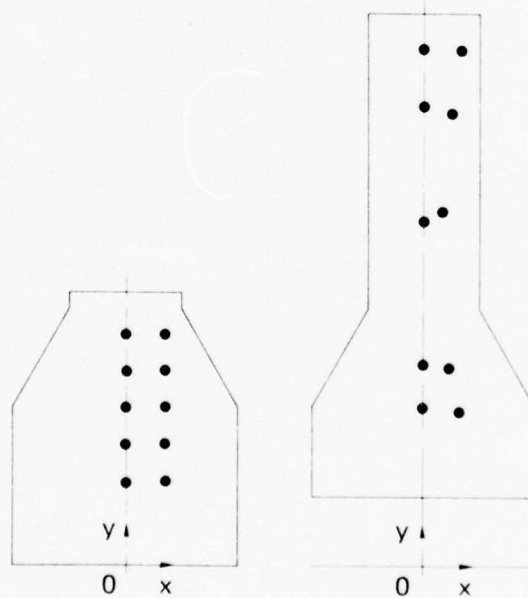
SHOT 135

MA-3701-142

FIGURE 31   INITIAL AND FINAL PARTICLE LOCATIONS FROM
GROUP 1 TEST 135

45
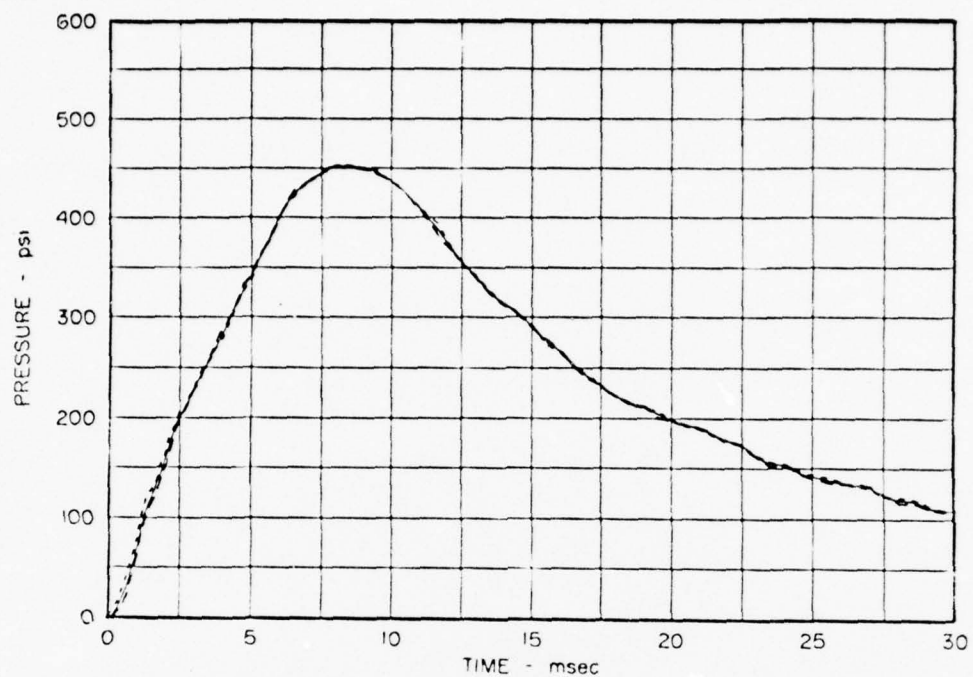
FIGURE 32   PRESSURE PULSES FROM FRICTION TEST 111
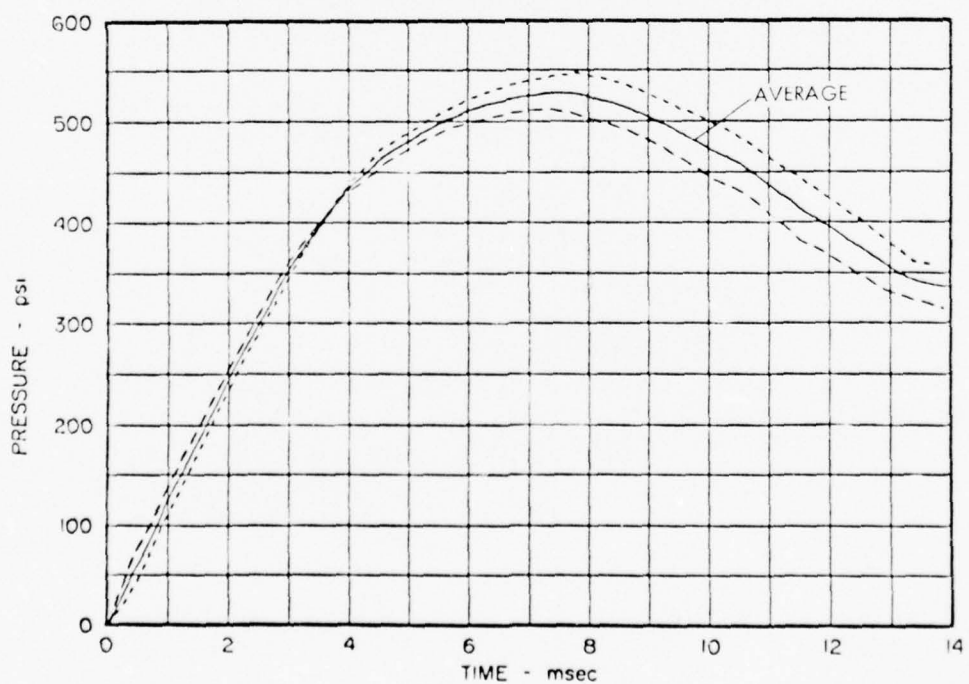
FIGURE 33   PRESSURE PULSES FROM FRICTION TEST 121

46
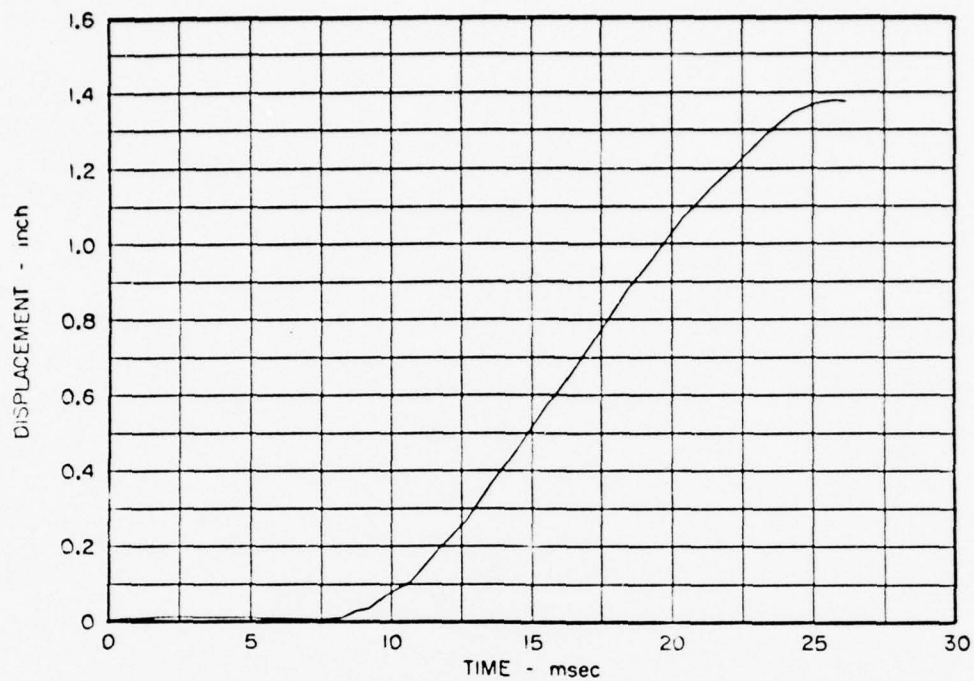
FIGURE 34   PISTON DISPLACEMENT FOR FRICTION TEST 111
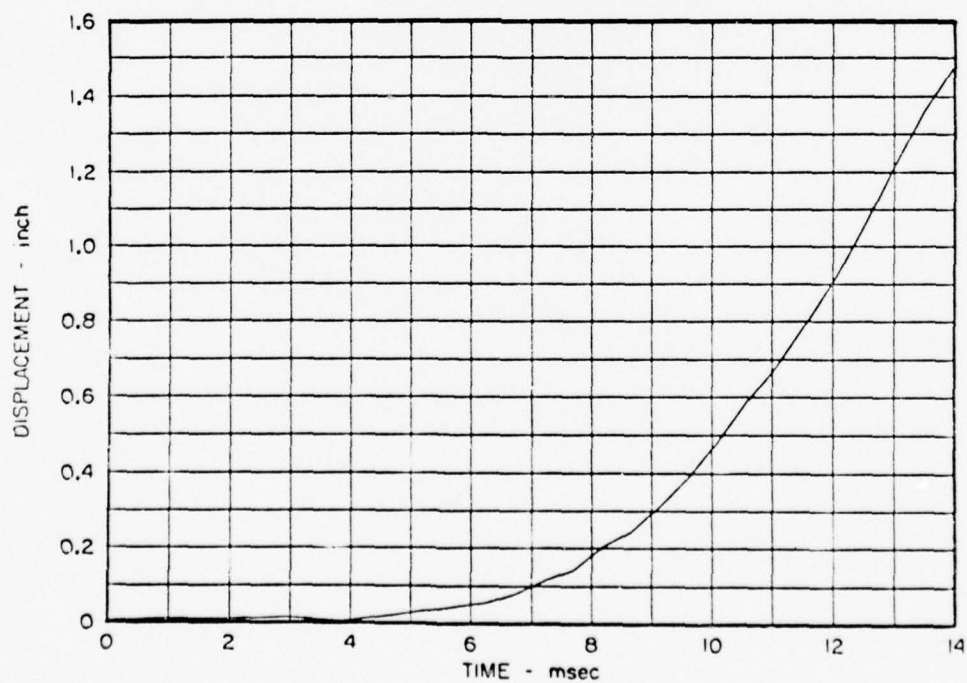
FIGURE 35   PISTON DISPLACEMENT FOR FRICTION TEST 121
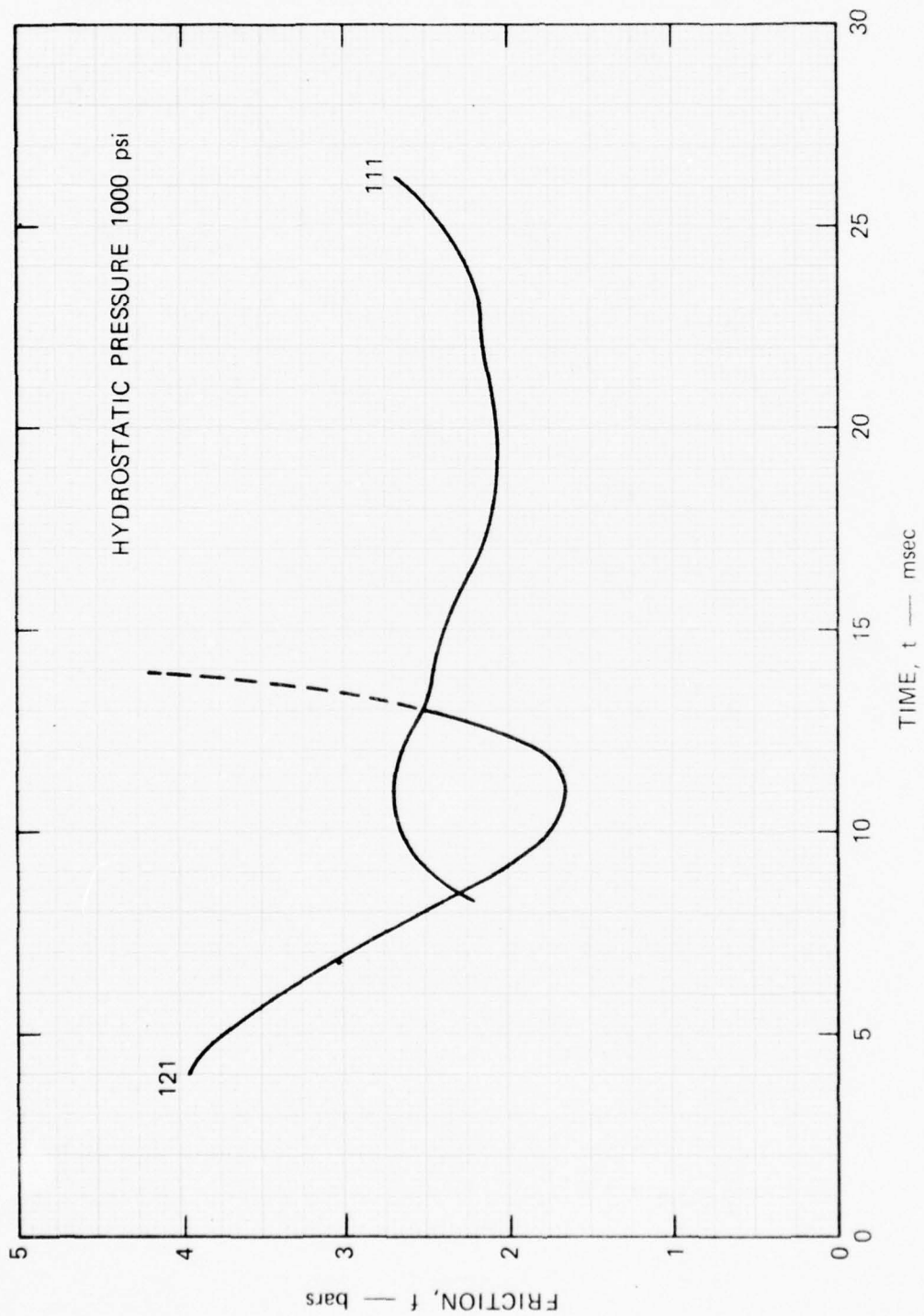
FIGURE 36   FRICTION RESULTS FROM TESTS 111 AND 121

MP-3702-154

48

Table 5

SLG PHYSICAL PROPERTIES

Test Sample	Densities (gm/cm^3)			Water % (Wet Weight)	Porosity %	Saturation %	Air Voids %	Unconfined Crush Strength psi
	Aged	Dry	Grain					
134 135	1.75	1.32	2.59	24	49	88	6	124
140 141 142 143	1.70	1.36	2.57	20	47	73	13	156
134[a]	1.74	1.30	2.59	25.3	50	88	6	
135[a]	1.74	1.30	2.59	24.7	49	88	6	
111	1.80	1.34	2.58	25	48	96	2	155
158 159	1.76	1.33	2.59	25	49	88	6	166 174

[a]Samples from extruded grout.

49

Table 6

MIXTURE FOR SUPERLEAN GROUT HSSL–1A

[a]Nevada Test Site Fines   72.5 %

  Type G Portland Cement   3.2 %

  Bentonite (Gel)   2.3 %

[b]CFR 2   0.03%

  Water   22.0 %

[a]Material passing through No. 7 sieve
(retains 2.5 mm dia particles).

[b]Concrete friction reducing compound 2
(detergent powder).
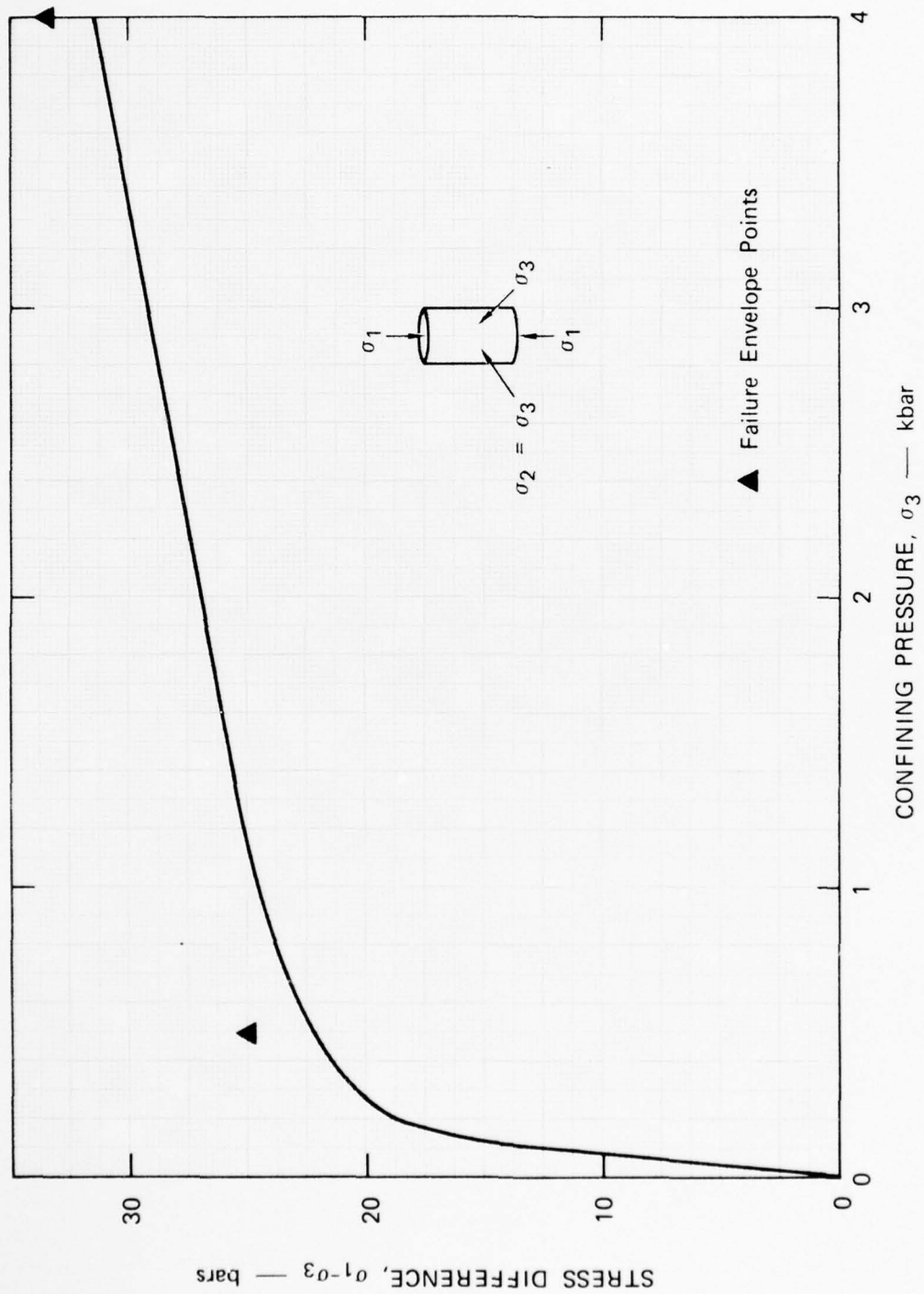
MP-3702-147

FIGURE 37   STRENGTH PROPERTIES OF SLG (UNIAXIAL STRAIN)

51
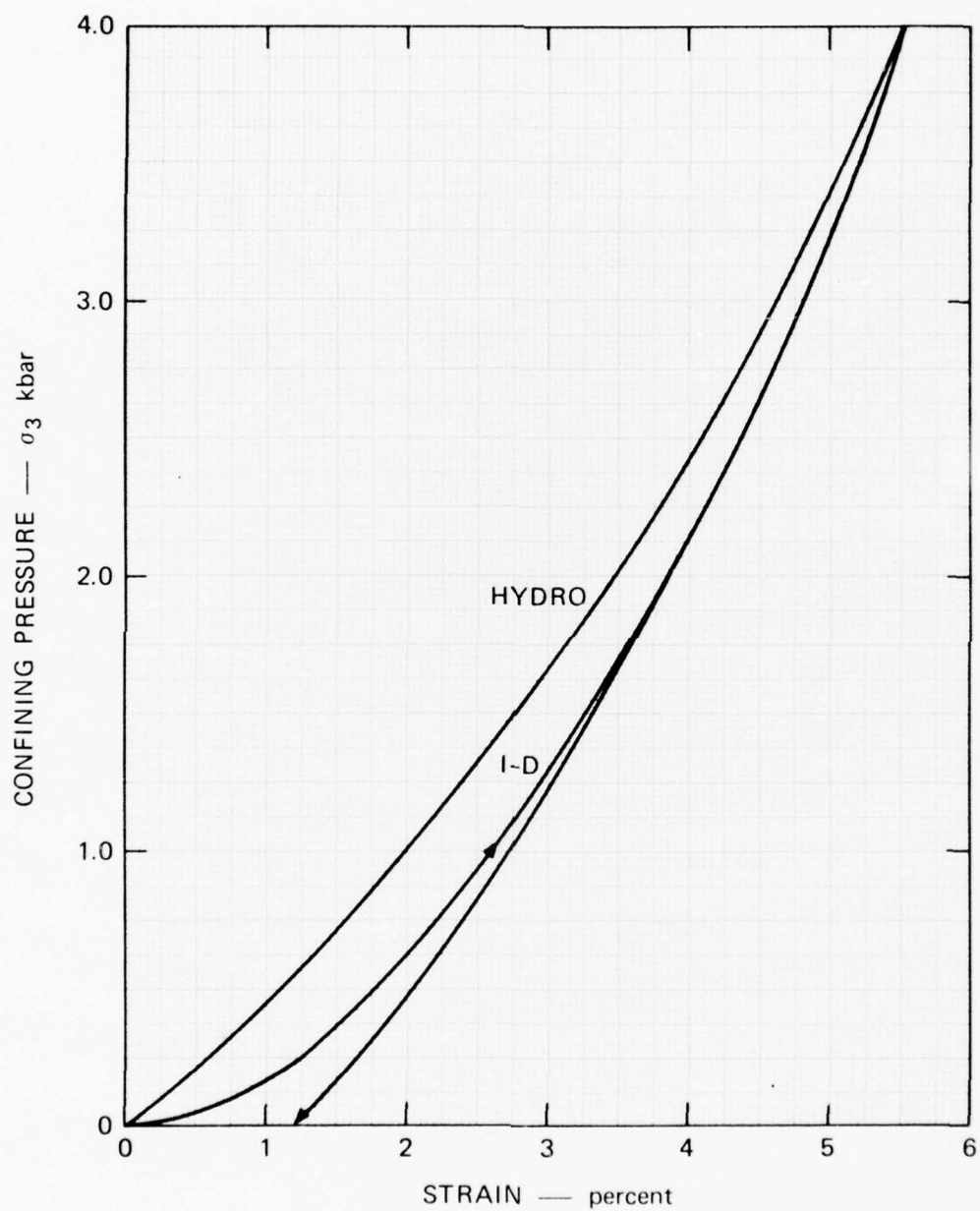
FIGURE 38   STRENGTH PROPERTIES OF SLG

MP-3702-148

52

Table 7

SIZE DISTRIBUTIONS OF NEVADA TEST SITE FINES FOR SIX SAMPLES

Particle Diameter (mm)	Percentage[a]					
	1	2	3	4	5	6
2.00	73.3	87.1	77.5	86.1	72.2	77.0
1.19	56.0	64.7	60.9	72.6	58.5	62.8
0.50	25.7	29.5	30.0	38.3	30.4	33.1
0.23	11.8	14.7	14.6	19.1	15.3	16.9
0.15	7.6	10.2	8.7	12.5	10.4	11.4

[a]Example: In Sample 3,
                      77.5 wt% of the total sample
                      passed through a sieve that
                      retains particles larger than
                      2 mm diameter,

                      60.9 wt% of the total sample
                      passed through a sieve that
                      retains particles larger than
                      1.19 mm diameter, and so on.

Table 8

DESIGN DISTRIBUTIONS OF NEVADA TEST SITE FINES

Particle Diameter (mm)	Percentage[a]		
	Average	Coarse	Very Coarse
2.0	80	72	70
1.19	60	55	45
0.50	30	26	20
0.23	16	11	10
0.15	10	8	5
	Unconfined Crush Strength (psi)		
	87	110	166
	107	134	185
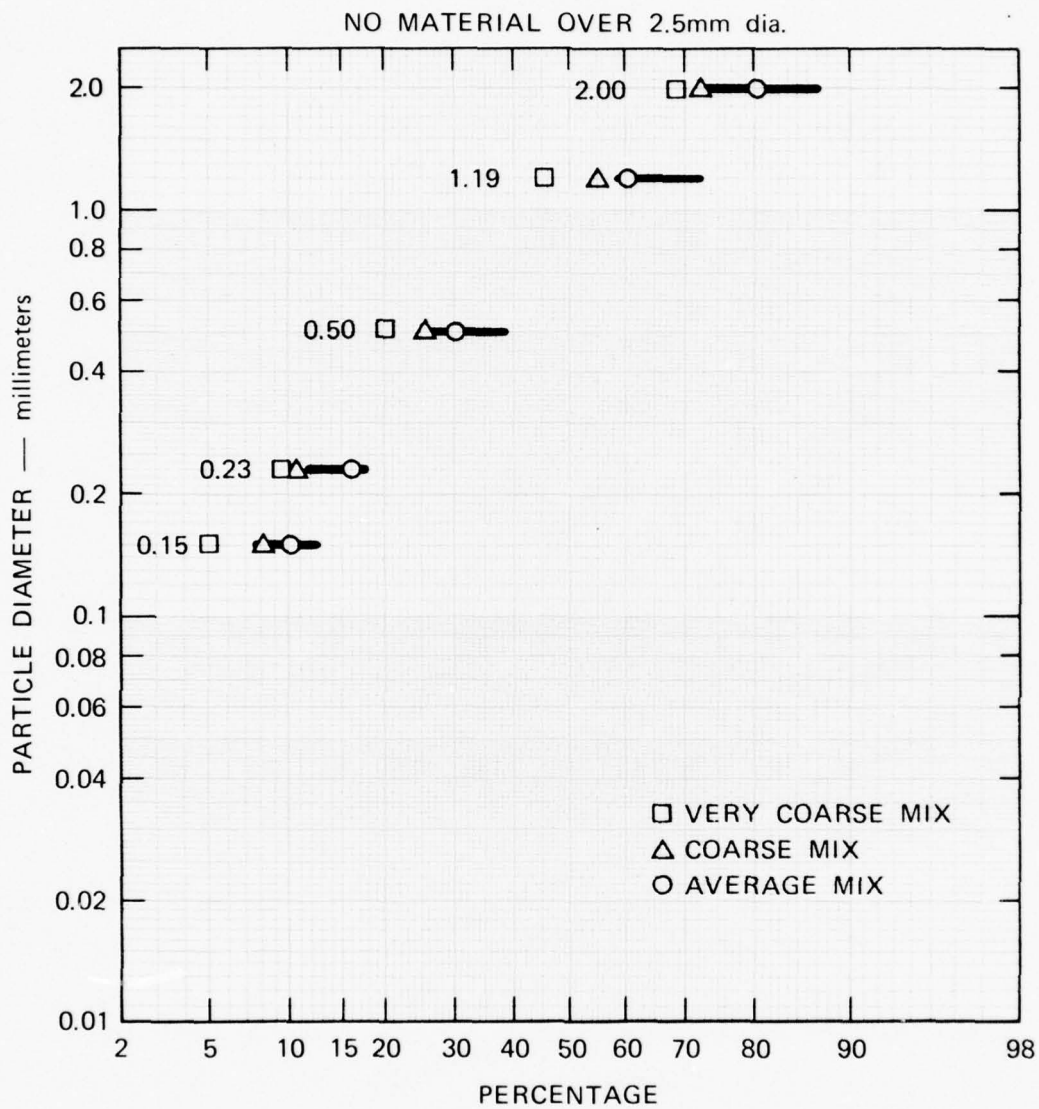
FIGURE 39   CUMULATIVE PARTICLE SIZE DISTRIBUTION FOR NEVADA TEST SITE FINES

55

IV   CONTAINMENT EXPERIMENTAL RESULTS

Table 9 lists the principal constant flow rate hydrofracture tests
conducted on 12-inch-diameter RMG spheres under 1000 psi overburden pres-
sure with either exploded or unexploded cavities. The tests may be
divided into three groups:

1. Tests 150 to 153 for obtaining the fracture pressure in
    an unexploded cavity.

2. Tests 154 and 155 for obtaining the fracture pressure
    in an exploded cavity.

3. Tests 160 to 163 for obtaining the local fracture
    pressure away from the cavity.

Comparison of results within each group, provides a measure of reproduci-
bility. An overall quantitative measure of the effect of a residual stress
field on the ability of the material to contain cavity gases is obtained
by comparing the maximum cavity fracture pressures of the first and second
groups. These values are 1670 and 2480 psi, respectively; thus, the resi-
dual stress field increases the fracture pressure by about 50% in these
tests.

Unexploded Cavity Tests 150-153 were conducted in the configuration
of Figure 40. The pressure-flow plots of Figure 41 were constructed from
the complete hydrofracture records, to allow an assessment of reproduci-
bility; plotting continued until flow was stopped. The fracture pressures
are listed in Table 9 as 1680, 1645, 1640, and 1710 psi with an average
of 1670 psi. The quantity of fluid pumped in at a flow rate of 4.26 cm^3/minute
ranges from 7.8 to 9.4 cm^3 at fracture, the total system volume being about
91 cm^3 (Table 1). Compressibility of a fluid with a bulk modulus of
330,000 psi accounts for only 0.46 cm^3 of the total volume at 1700 psi.

Treating the RMG sphere as an elastic material of shear modulus
$G = 10^6$ psi about to yield with an internal pressure of $P_s = 1700$ psi

56

and a pressure at infinity of P_∞ = 1000 psi, gives an estimate of only 0.016 cm^3 for the increase in cavity volume before fracture. The piping system with gages can absorb about 2.5 cm^3 at 1700 psi. Thus, most of the fluid is being forced either into the rock pores from the cavity wall or around the access pipe.

As shown in Figure 41, the cavity pressure drops rapidly following fracture, because fluid can now flow into the thin plane of the crack. The minimum pressure ranges from 1100 to 1300 psi. A gradual rise in pressure follows, implying resistance to hydrofracture; after 25 cm^3 of flow, the pressures range from 1150 to 1450 psi.

The sphere was removed from the pressure vessel after release of the internal pressure followed by release of the overburden pressure. In each case, a crack was visible around almost the entire circumference. The two halves were tapped apart by use of a broad chisel. Figure 49 shows the exposed fracture plane and the extent of the dyed Glycerin fluid in Test 150. Fracture occurred out of the plane of the access pipe; thus, the pipe probably does not introduce a stress concentration for crack initiation. For comparison with the fracture behavior in the presence of a residual stress field note that the flow is from the cavity outward and surrounds the cavity in a fairly uniform manner.

The configuration of Figure 42 was used in Exploded Cavity Tests 154 and 155. The pressure-flow plots of Figure 43 were constructed from the complete hydrofracture records to allow an assessment of reproducibility; plotting continued until flow was stopped. Fracture occurs at 2500 and 2060 psi and the maximum pressures achieved are 2460 and 2620 psi. The quantities of fluid pumped in at a flow rate of 4.26 cm^3/minute are 3.5 and 6 cm^3. These values are below the range of 7.8 to 9.4 cm^3 for the Unexploded Cavity Tests 150 and 153, implying that the material around the exploded cavity is less permeable because of crushing of the pores.

In both tests, the pressure drops by about 100 psi after fracture, considerably less than in Tests 150 to 153. This pressure drop implies that the extent of initial fracture is reduced by the compressive residual

stress field. The pressure now rises steeply to exceed the initial fracture pressure, probably because of the compressive stress field resistance to crack propagation. In Test 154, it appears as if a second fracture is initiated at a pressure of 2450 psi and a fluid flow of 7 cm^3. The pressure then drops by 150 psi and gradually increases to 2460 psi at about 15.7 cm^3 before suddenly dropping to 1400 psi. In Test 155, an apparent second fracture does not occur. The pressure rises to its maximum at 2620 psi and drops suddenly to 1300 psi at about 10.5 cm^3. The sudden pressure drops are attributed to the cracking breaking through highly compressive residual stress field.

The sphere was removed from the pressure vessel after release of the internal pressure followed by release of the overburden pressure. In each case, a crack was visible around almost the entire circumference. The two halves were tapped apart by use of a broad chisel. Figure 50 shows the exposed fracture plane and the extent of the dyed Glycerin fluid in Test 155. The dyed fracture area surrounds the cavity circle but lies outside an irregular annular region of unfractured material that coincides with the region of compressive residual stress. The exposed fracture plane is intersected by another orthogonal fracture plane. This second plane is dyed and intersects the cavity.

The photographs of Figure 48 show the corresponding results for Test 146, an earlier test performed at a slower flow rate (0.71 cm^3/minute). The dyed region is less extensive but the character is the same, a breaking through of the high residual stress field region adjacent to the cavity followed by spreading hydrofracture in the low residual stress field region beyond.

The configuration of Figure 44 was used in Exploded Cavity Tests 160 and 161. The pressure-flow plots of Figure 45 were constructed from the complete hydrofracture records to allow comparison. As shown in Figure 44, local pressurization of the grout away from the cavity is effected through four 1/8-inch-diameter holes in the access tube. The pressurization location is outside the region of predicted maximum residual stresses. Figure 45 shows that the pressure histories are highly

58

oscillatory in these two tests and that the general pressure levels are different. This behavior probably stems from the highly localized complicated configuration where the grout is pressurized, providing many stress concentration zones for local crack initiation. Figure 51 shows the main fracture plane for Test 161. The dyed region indicates that the crack was forced to spread around the central spherically annular region of high compressive residual stress. A feature not previously observed appears in Figure 51: a crack that is approximately spherical, almost surrounding the cavity but located eccentrically; this feature was not observed in Test 160. Formation of such a circumferential crack is consistent with the residual stress field in this region where the radial stress component is predicted to be less compressive than the tangential stress component.

The configuration of Figure 46 was used in Exploded Cavity Tests 162 and 163. The pressure-flow plots of Figure 47 were constructed from the complete hydrofracture records to allow comparison. The configuration for local pressurization of the grout away from the cavity provides an exposed cylindrical grout surface 1/4 inch in diameter and 1 inch long; the objective was to simplify the configuration of Figure 44 for Tests 160 and 161. Figure 47 shows that the pressure histories are oscillatory with differing pressure levels, but the results show a marked improvement over those of Figure 45, with less oscillation and smaller pressure difference (2000 and 2300 psi). Figure 52 shows the main fracture plane for Test 163. The plane is almost tangential to the cavity. The dyed region indicates that the crack was forced to spread around the central, spherically annular region of high compressive residual stress.

Figure 53, like Figure 41, shows the pressure-flow curves for the unexploded cavity Tests 150 to 153 augmented by the curve for Test 147, because the only parameter difference is the smaller cavity size (0.65 in diameter compared with 1.13 in diameter for Test 147). The fracture pressure of 1470 psi in Test 147 is lower but comparable with the average pressure of 1670 psi for Tests 150 to 153. Fracture occurred after about 5 cm^3 of flow, which is well below the 7.8 to 9.4 cm^3 range for Tests 150 to 153. This lower flow value is attributable to the smaller spherical surface area available for fluid flow into the grout pores.

59

Figure 54, like Figure 43, shows the pressure-flow curves for the exploded cavity Tests 154 and 155 augmented by the curve for Test 146, because the only parameter difference is the smaller flow rate (0.71 cm^3/minute compared with 4.26 cm^3/minute) for Test 146. The fracture pressure for Test 146 is similar to that for Test 155 (2540 and 2500 psi), and the overall pressure history is similar. The interesting difference is the greater fluid flow that occurs before fracture in Test 146, specifically, 24 cm^3 compared with about 4 and 6 cm^3 in Tests 154 and 155. The greater flow is caused by the slower imposed flow rate allowing a greater volume of flow into the grout pores.

Table 9

SUMMARY LIST OF CONSTANT FLOW RATE TESTS[a]

Test	Cavity Dia Before (in.)	Cavity Dia After (in.)	Explosive Weight (gm)	Maximum Pressure (psi)	Configuration Type[b]	Figure	
146	0.65	1.16	1	2540	A	10,16	Exploded cavity pressurization (slow rate: 0.71 cm^3/min)[c]
150	1.13	1.13	-	1680	A	8,9,17,A-3	Unexploded cavity pressurization
151	1.14	1.14	-	1645	A	8,9,A-4	Repeat of 150
152	1.10	1.10	-	1640	A	8,9,A-5	Repeat of 150
153	1.15	1.15	-	1710	A	8,9,A-6	Repeat of 150
154	0.65	1.12	1	2460	A	10,11,A-7	Exploded cavity pressurization
155	0.65	1.10	1	2500	A	10,11,18, A-8	Repeat of 154
160	0.65	1.15	1	2070	B	12,13,A-9	Far-field local pressurization (no cavity pressure)
161	0.65	1.15	1	3260	B	12,13,A-10	Repeat of 160
162	0.65	1.08	1	1970	B	14,15,A-11	Far-field local pressurization (no cavity pressure)
163	0.65	1.15	1	2320	B	14,15,A-12	Repeat of 162

[a]Overburden pressure 1000 psi.

[b]Type A for pressurization in cavity; Type B for local pressurization away from cavity.

[c]Flow rate in remaining tests, 4.26 cm^3/min.

61

CONSTANT FLUID
FLOW RATE

STEEL TUBE (3/8 in. OD)

12 in. dia
RMG SPHERE

~1-1/8 in. dia
SPHERICAL
CAVITY

WATER
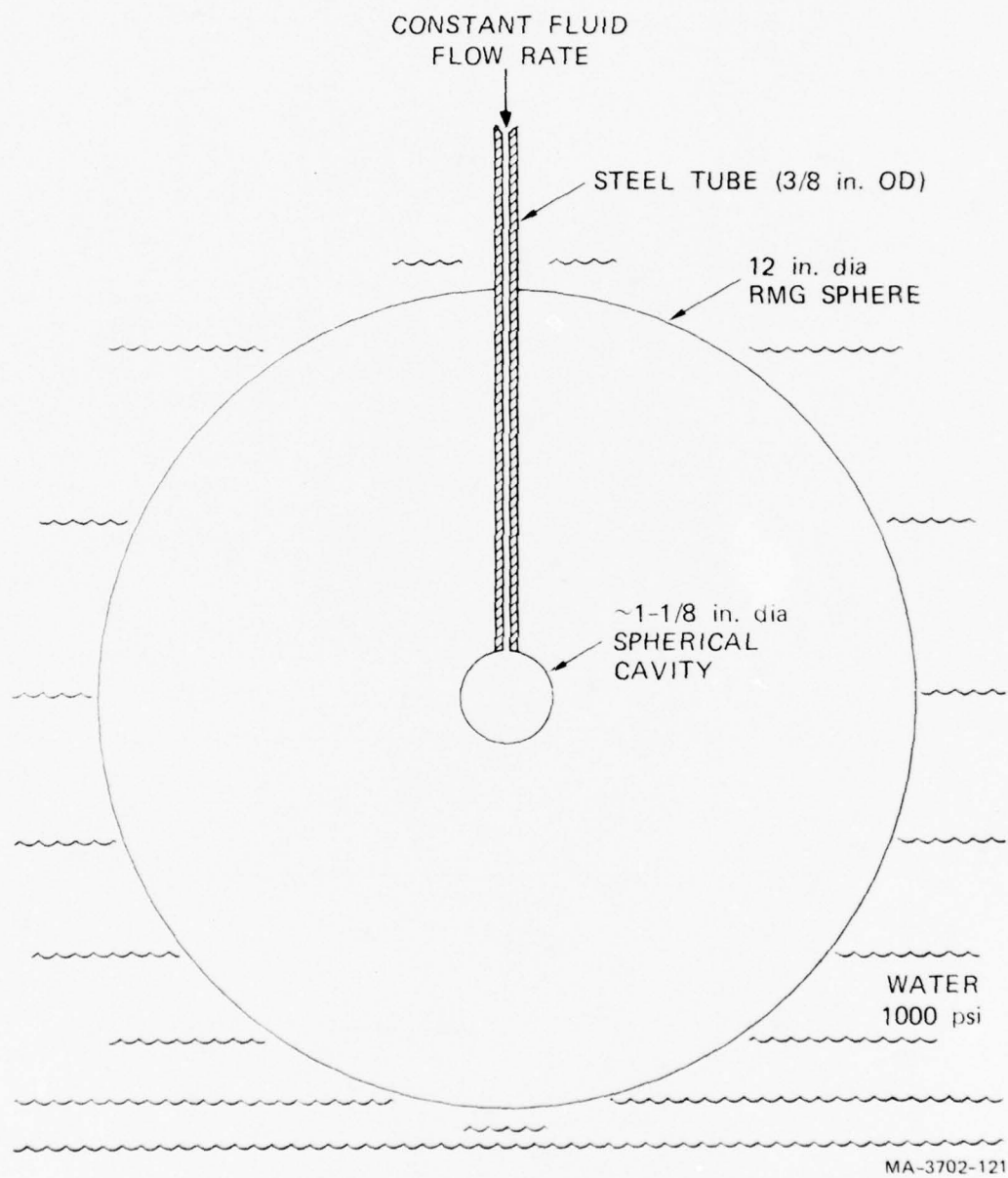1000 psi

MA-3702-121

FIGURE 40   CONFIGURATION FOR UNEXPLODED CAVITY TESTS 150-153
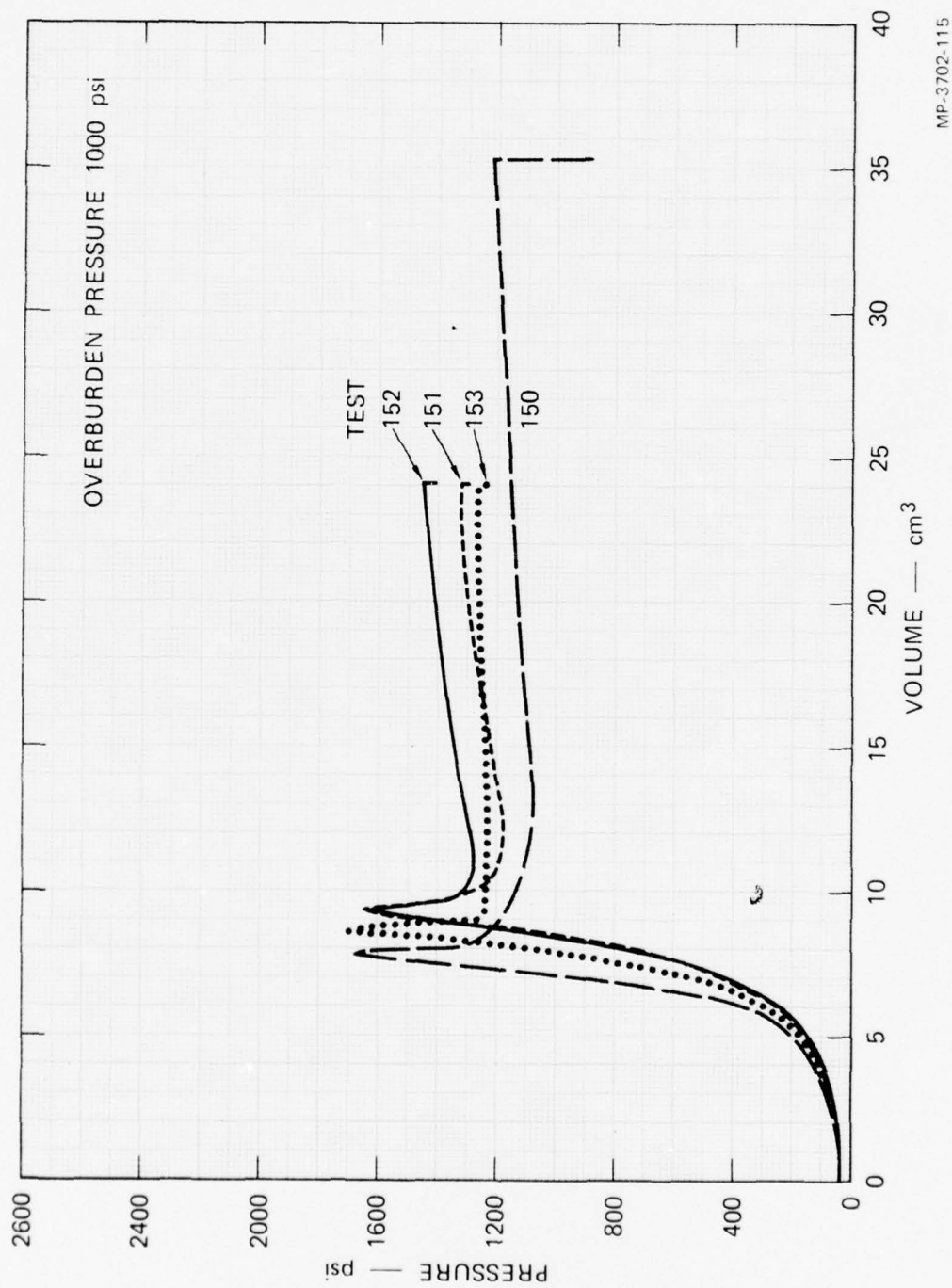
FIGURE 41   HYDROFRACTURE PRESSURES FOR UNEXPLODED CAVITY TESTS 150-153

MP-3702-115

63

CONSTANT FLUID
FLOW RATE

STEEL TUBE (3/8 in. OD)

12 in. dia
RMG SPHERE

EXPLODED SPHERICAL
CAVITY
(~1-1/8 in. dia)

ORIGINAL SPHERICAL
CAVITY (0.65 in. dia)

WATER
1000 psi

MA-3702-122

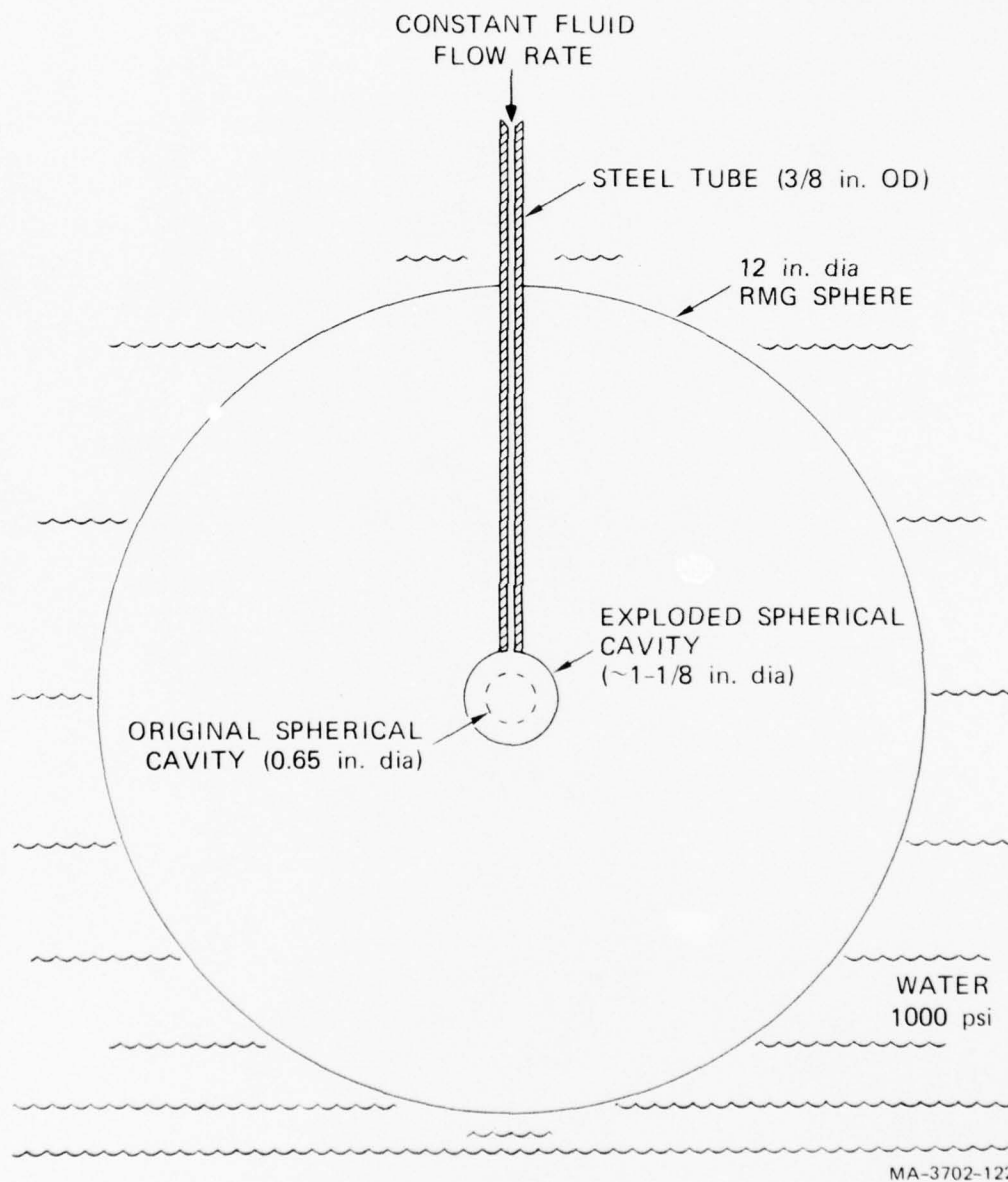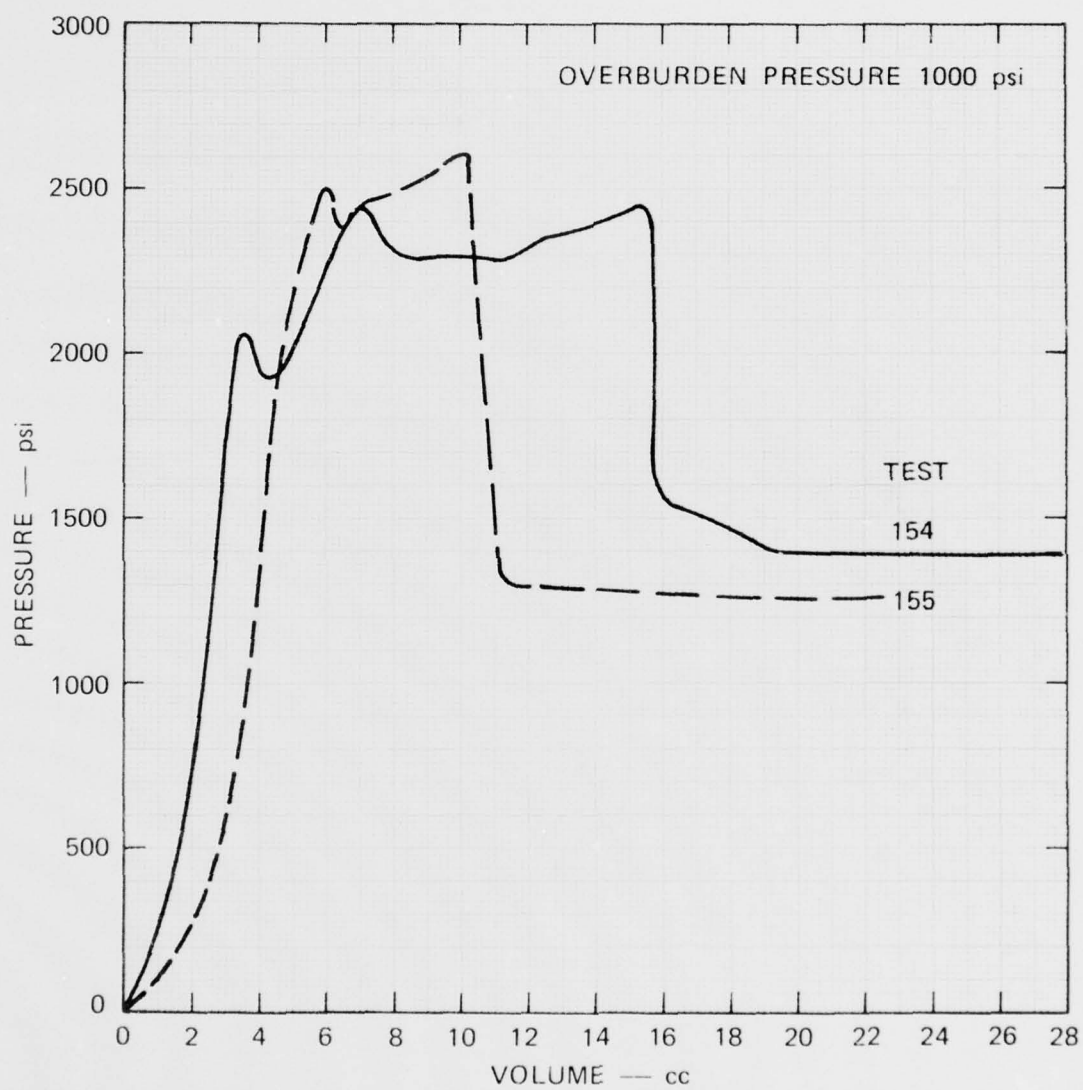FIGURE 42   CONFIGURATION FOR EXPLODED CAVITY TESTS 154 AND 155

64

FIGURE 43   HYDROFRACTURE PRESSURES FOR EXPLODED CAVITY TESTS 154 AND 155

MP-3702-114

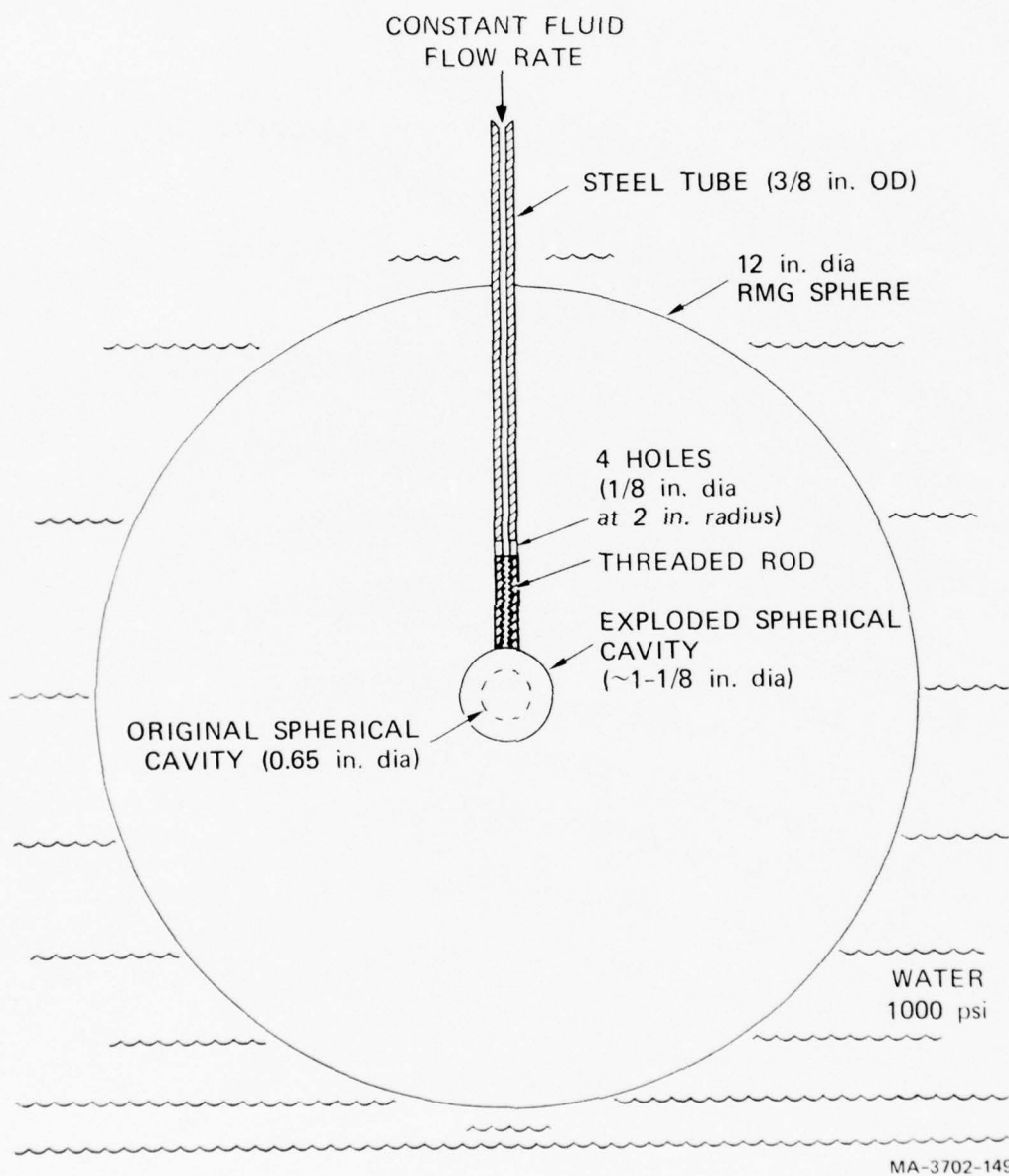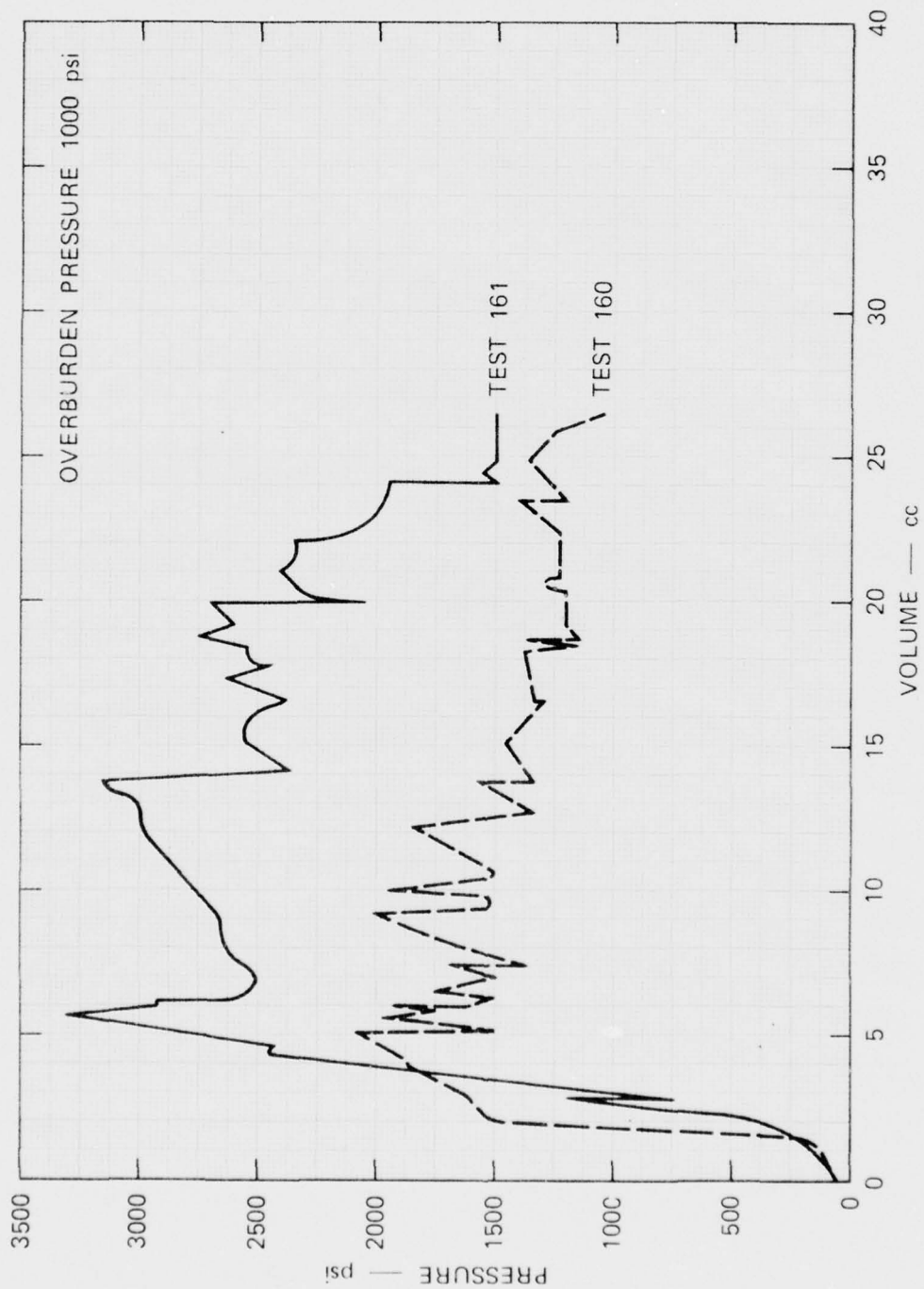FIGURE 44   CONFIGURATION FOR EXPLODED CAVITY TESTS 160 AND 161

66

FIGURE 45 HYDROFRACTURE PRESSURES FOR EXPLODED CAVITY TESTS 160 AND 161

MP-3702-123

67

CONSTANT FLUID
FLOW RATE

STEEL TUBE (3/8 in. OD)

12 in. dia
RMG SPHERE

1 in.

HYDROCAL

EXPLODED SPHERICAL
CAVITY
(~1-1/8 in. dia)

ORIGINAL SPHERICAL
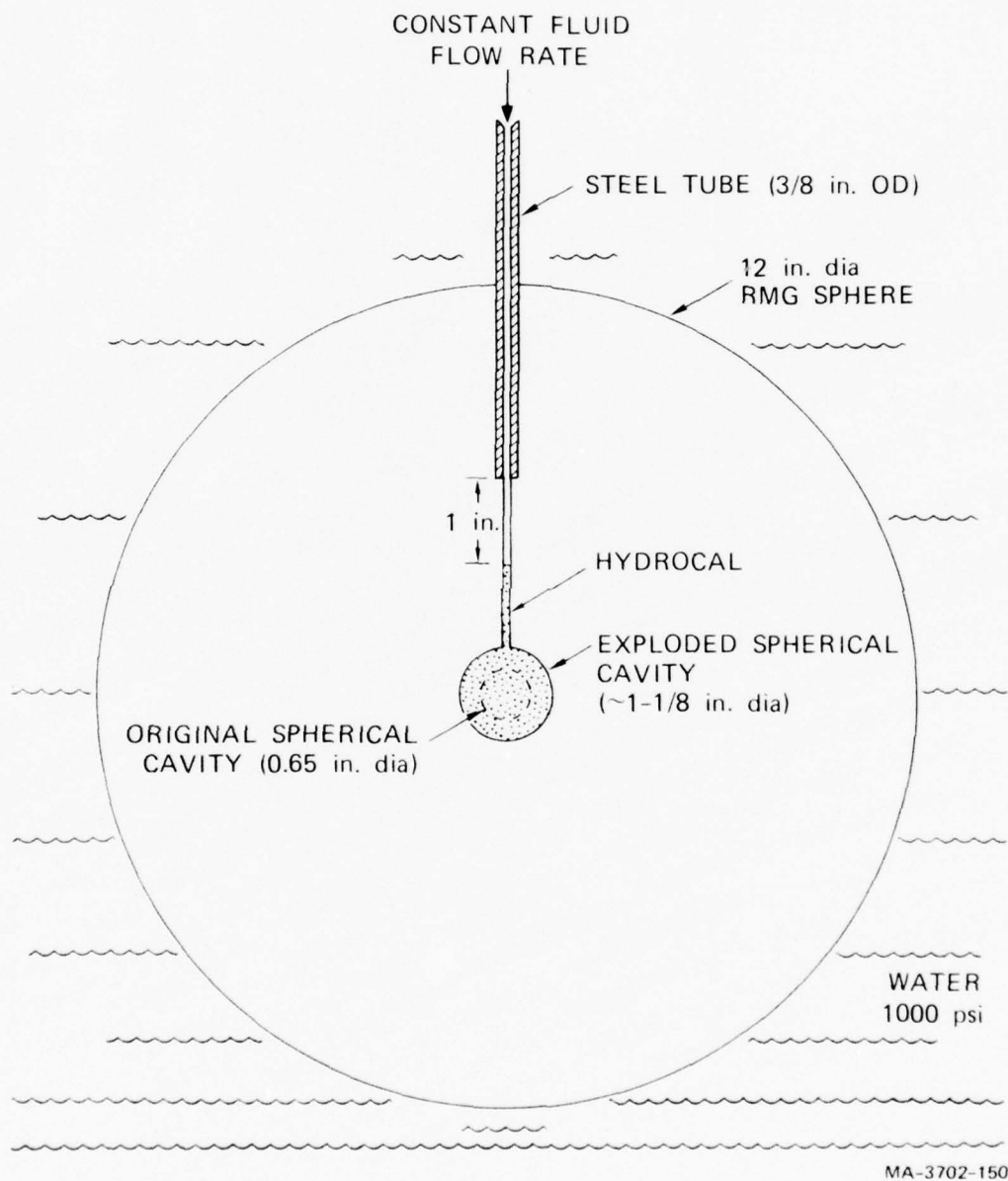CAVITY (0.65 in. dia)

WATER
1000 psi

MA-3702-150

FIGURE 46   CONFIGURATION FOR EXPLODED CAVITY TESTS 162 AND 163
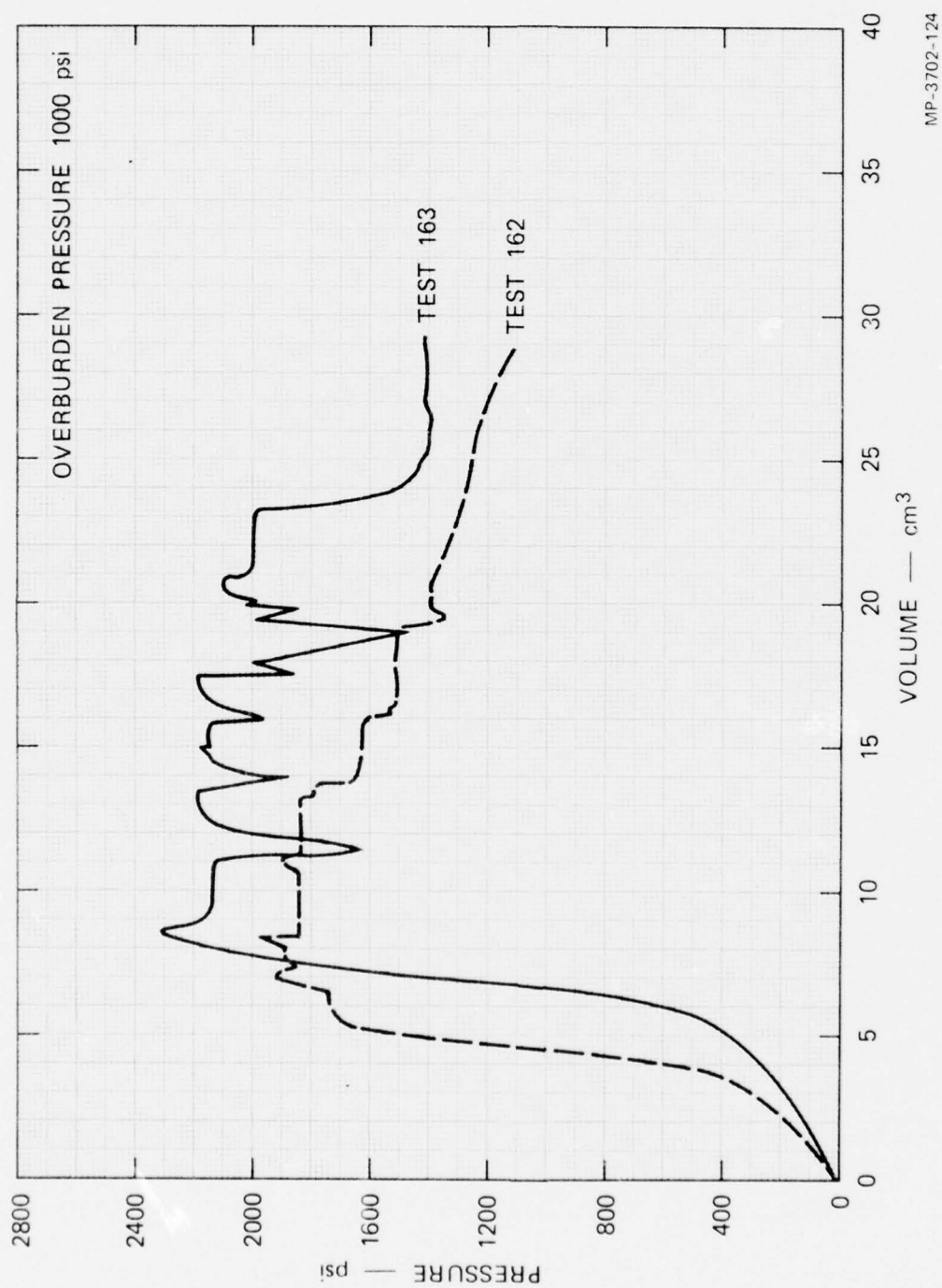
68

FIGURE 47   HYDROFRACTURE PRESSURES FOR EXPLODED CAVITY TESTS 162 AND 163
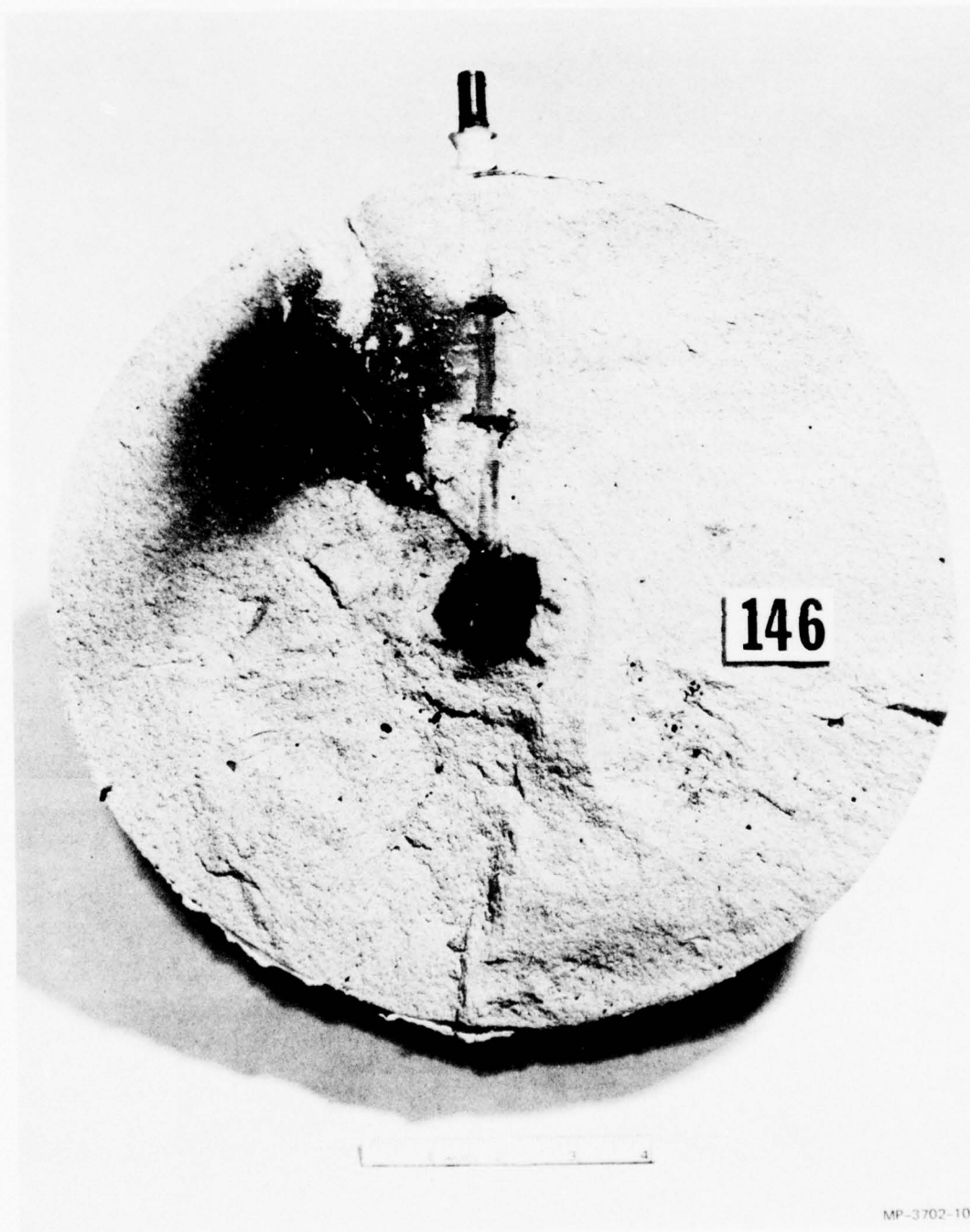
MP-3702-124

69

FIGURE 48   HYDROFRACTURE FROM AN EXPLODED CAVITY — TEST 146

MP-3702-109

70

MP-3702-110

FIGURE 48   HYDROFRACTURE FROM AN EXPLODED CAVITY — TEST 146 (Concluded)

150

MP-3702-106

FIGURE 49   HYDROFRACTURE FROM AN UNEXPLODED CAVITY — TEST 150

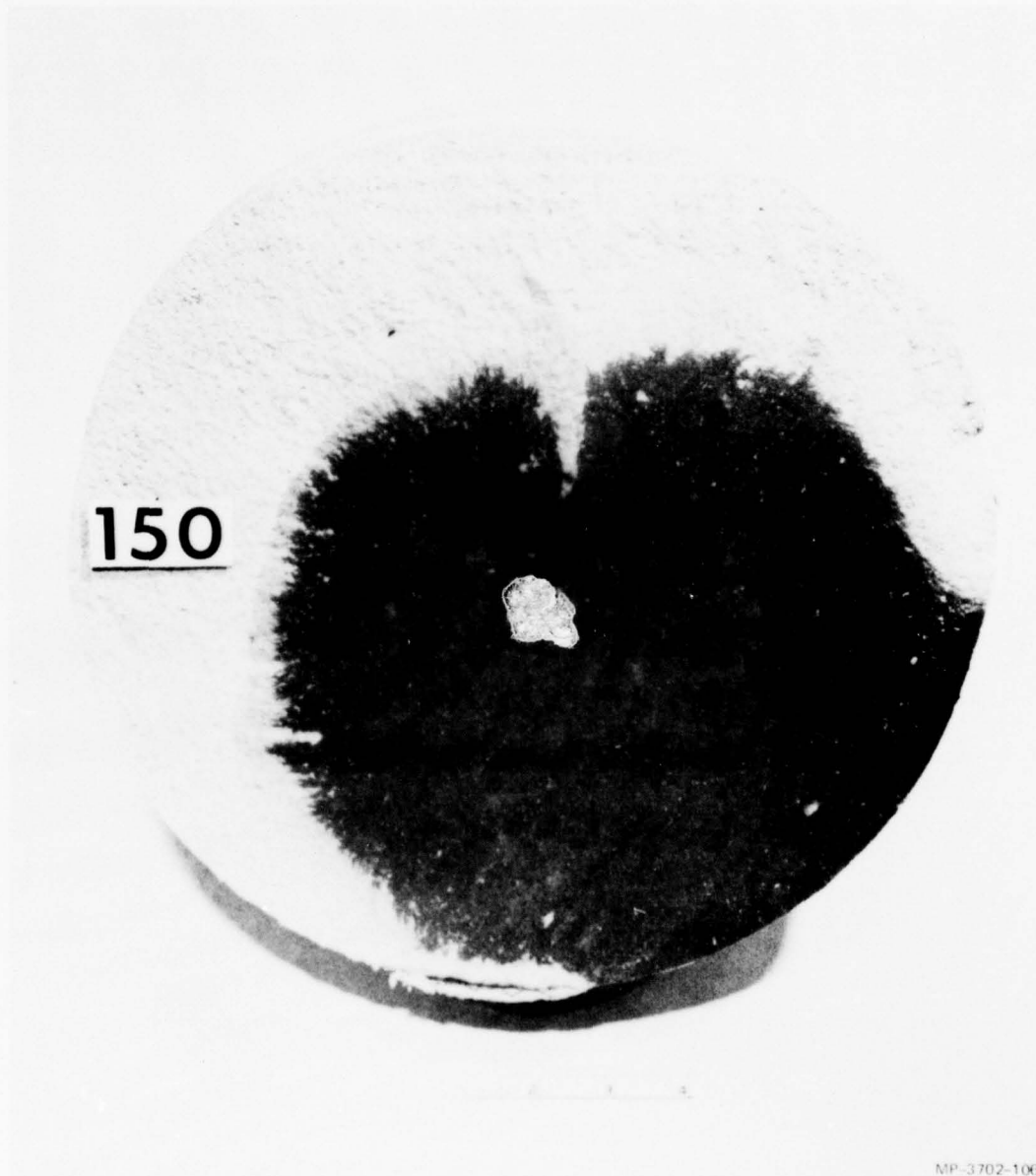FIGURE 49   HYDROFRACTURE FROM AN UNEXPLODED CAVITY — TEST 150 (Concluded)

FIGURE 50   HYDROFRACTURE FROM AN EXPLODED CAVITY — TEST 155

MP-3702-113

74

FIGURE 50   HYDROFRACTURE FROM AN EXPLODED CAVITY — TEST 155 (Concluded)

MP-3702-112

FIGURE 51   HYDROFRACTURE FROM LOCALITY AWAY FROM AN EXPLODED CAVITY
TEST 161

MP-3702-126

FIGURE 51   HYDROFRACTURE FROM LOCALITY AWAY FROM AN EXPLODED CAVITY —
TEST 161 (Concluded)

MP-3702-127

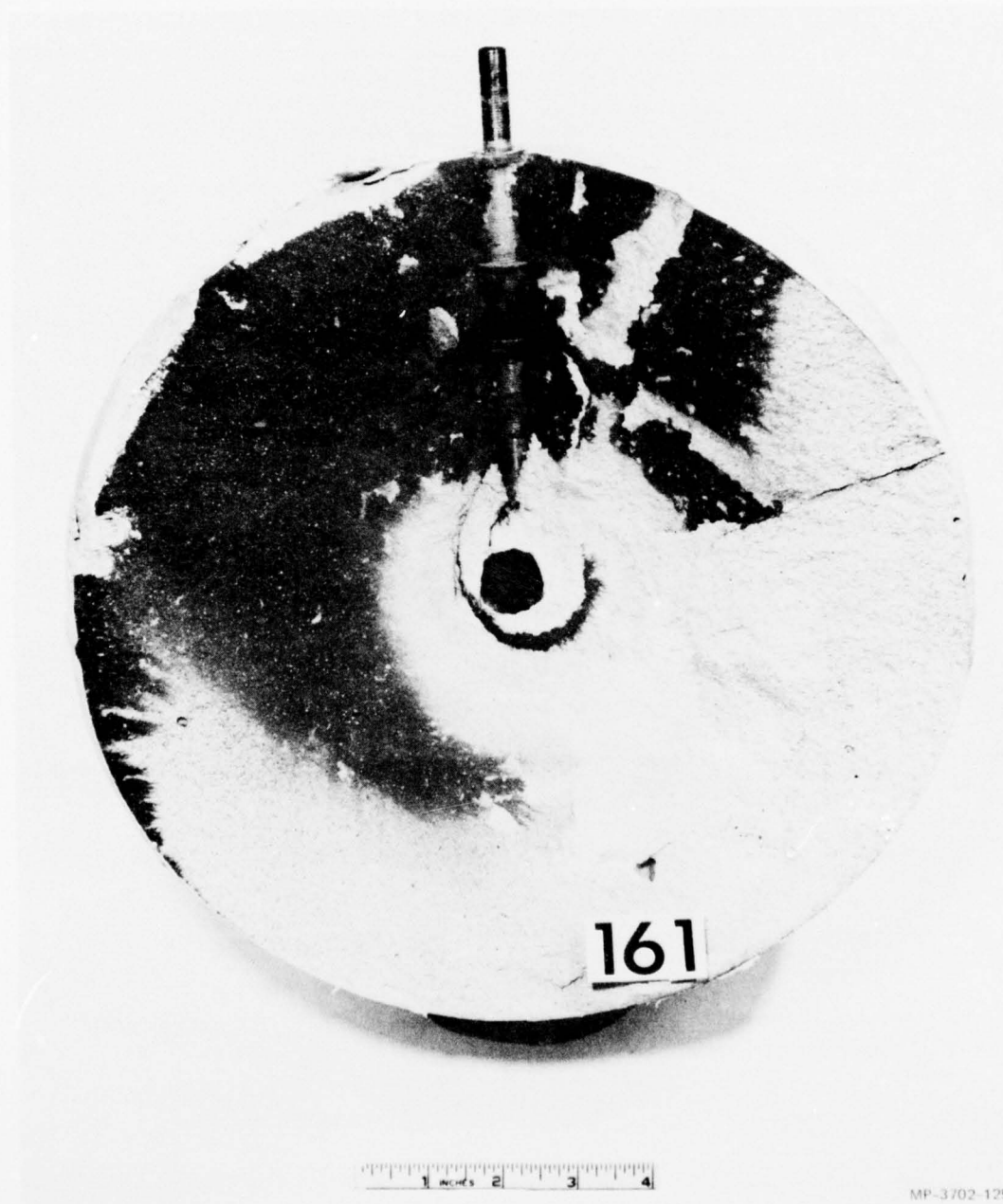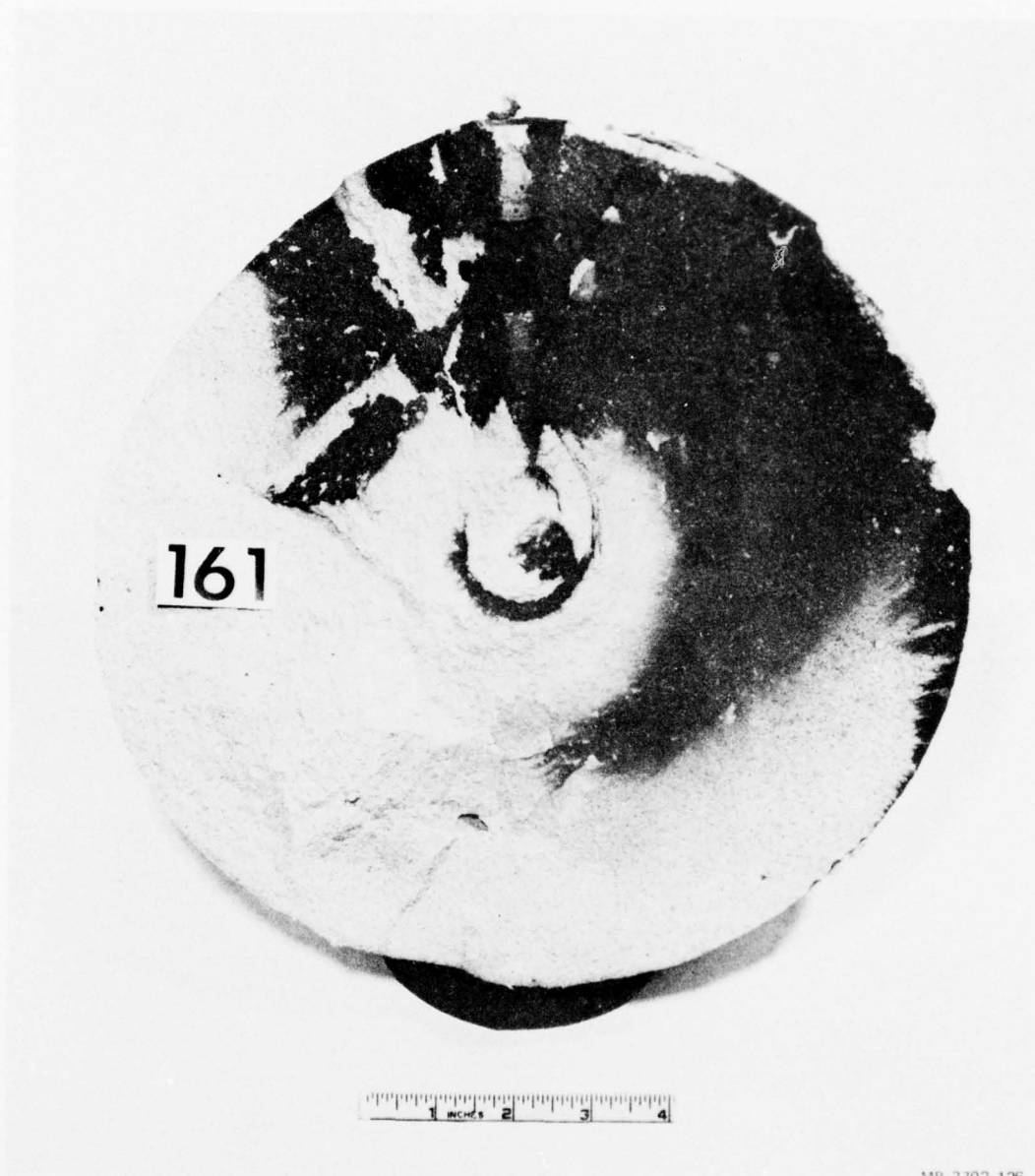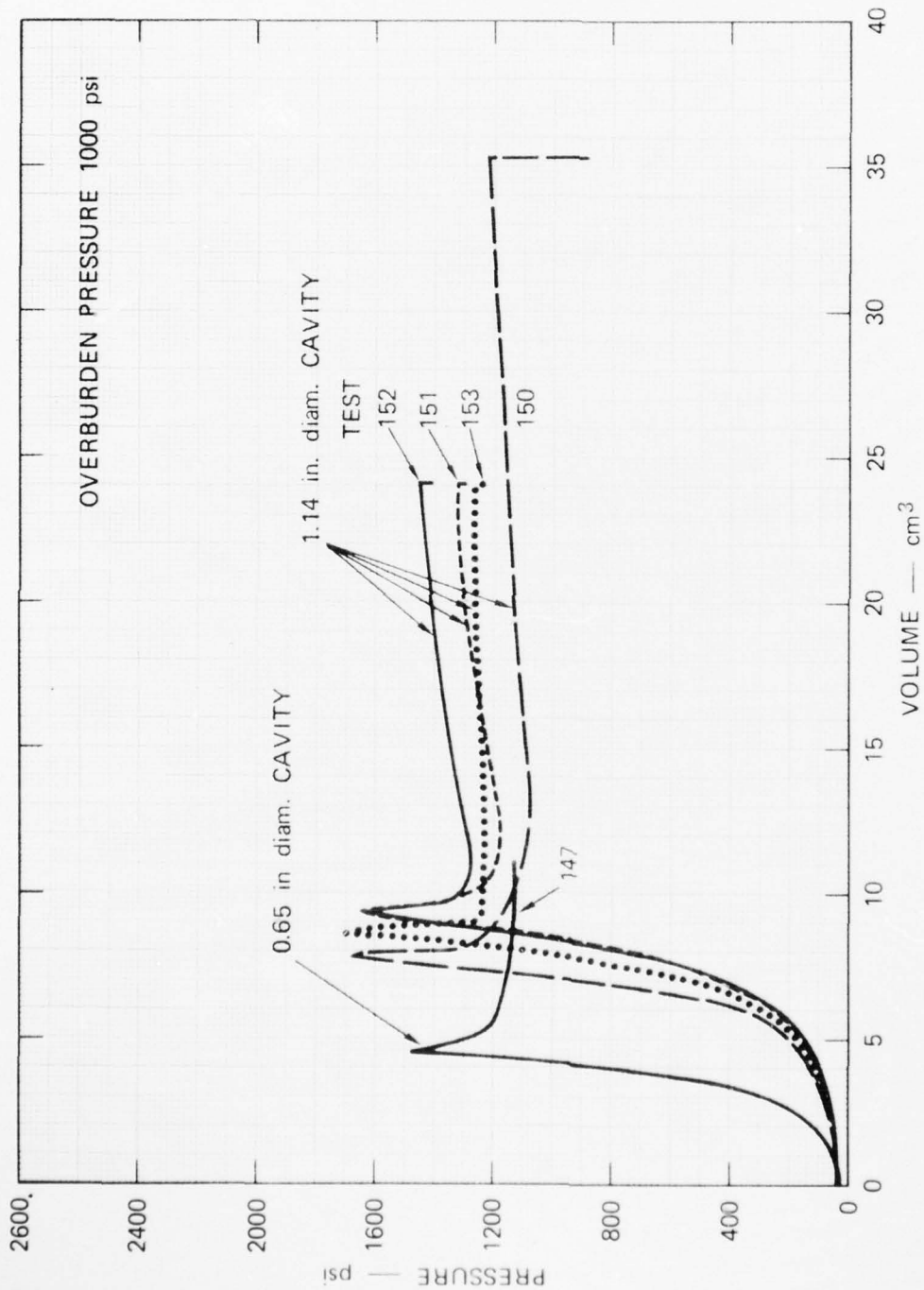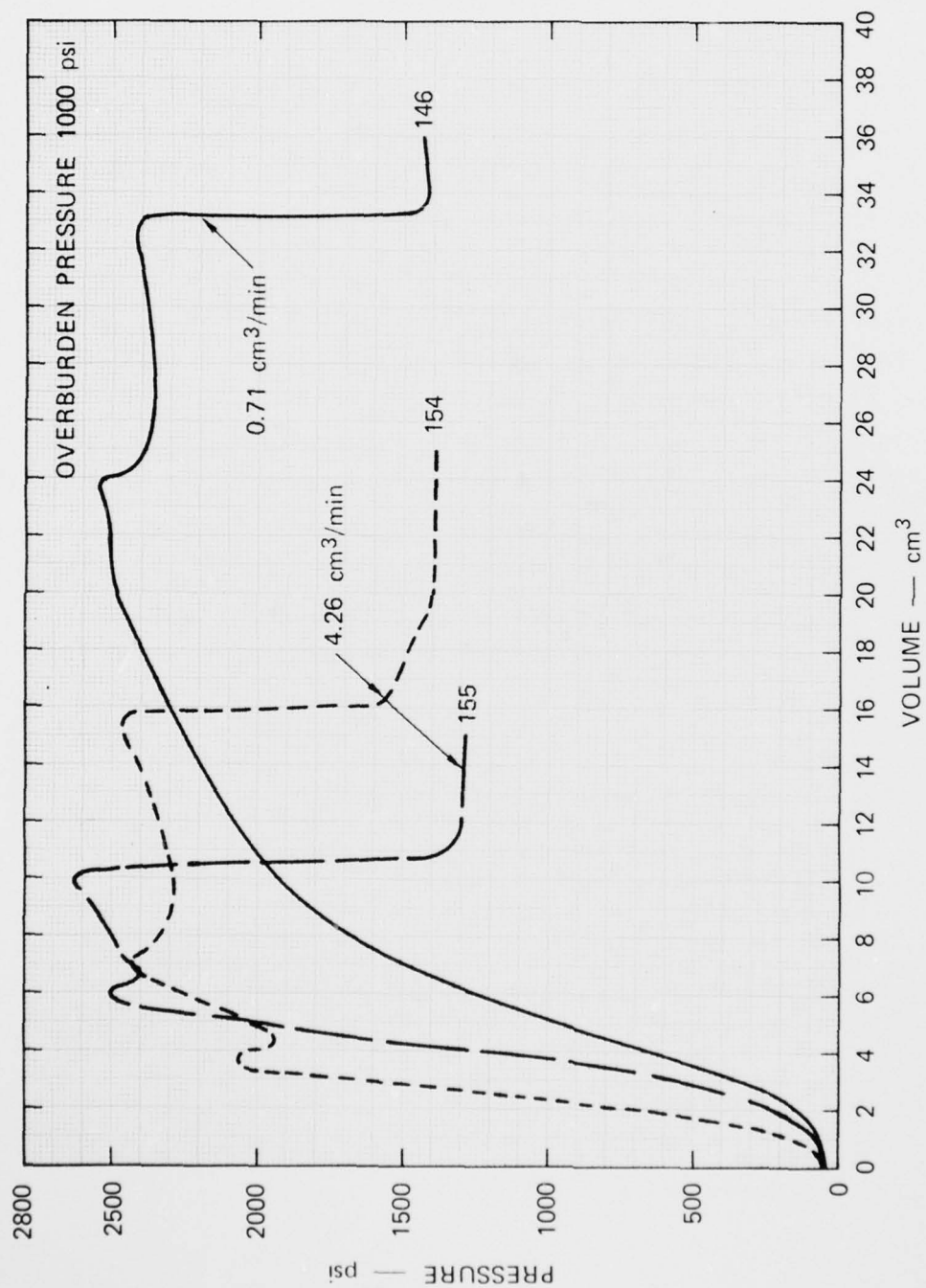FIGURE 52   HYDROFRACTURE FROM LOCALITY AWAY FROM AN EXPLODED CAVITY —
TEST 163

163

FIGURE 52   HYDROFRACTURE FROM LOCALITY AWAY FROM AN EXPLODED CAVITY —
TEST 163 (Concluded)

79

FIGURE 53 HYDROFRACTURE PRESSURES FOR UNEXPLODED CAVITY TEST 147 AND TESTS 150-153 — CAVITY VOLUME EFFECT

FIGURE 54   HYDROFRACTURE PRESSURES FOR EXPLODED CAVITY TESTS 146, 154, AND 155 — FLOW RATE EFFECT

MP-3702-153

81

V   CONTAINMENT ANALYSIS

SRI Topical Report 3702-2 presents an analytical treatment of the dynamic expansion of a spherical cavity caused by an explosive pressure pulse. The analysis was performed to describe formation of the residual stress field and to establish dependence of the field on the parameters involved.

The analysis is a simple extension of the work of Hopkins[10] to describe rebound and a second expansion phase. Numerical data were chosen to correspond to the laboratory containment experiments described in Sections II-B and IV. Predictions for the final cavity radius are compared with experimental results. Predictions for cavity expansion history and stress distributions are compared with the predictions of a finite-difference code. Formulas are provided for the final cavity radius in terms of the explosive energy supplied and for the maximum tensile tangential stress and maximum compressive radial stress together with their locations at the end of the first expansion phase.

From the numerical examples and manipulation of the governing equations the following observations are made.

- Cavity expansion and contraction compared favorably with finite-difference code predictions (code included compressibility).

- Stress distributions when the cavity was fully expanded and fully contracted showed qualitative agreement with the code predictions. Quantitative differences arise because of the smaller ranges reached by the elastic-plastic interface in the code description, because volumetric plastic work is allowed.

- The final to initial radius ratio compares reasonably well with the experimental ratio.

- The simplest formula for the upper bound of the final to initial radius ratio, a_2/a_0, is

$$a_2/a_0 = (\bar{w}/4.3\,Y)^{1/3}$$

where $\bar{w}$ is the average initial energy density in the cavity and Y is the yield stress of the surrounding material. The radial ratio is thus independent of the material density, shear modulus, and overburden pressure.

- The simplest formulas for the maximum tangential stress σ_t and the maximum compressive radial stress σ_r, together with their locations R_2 and r_m at the end of the first expansion phase, are

$$0.9 - P_\infty/Y < \sigma_t/Y < 1.0 - P_\infty/Y$$

$$R_2/a_2 = (2G/Y)^{1/3}$$

$$\sigma_r/Y = -0.8 - P_2/Y$$

$$2.0 < r_m/a_2 < 2.3$$

where P_2 is the cavity pressure when fully expanded.

- Maxσ_t and max$(-\sigma_r)$ are independent of density and shear modulus and are approximately linearly dependent on the yield stress.

- Maxσ_t is reduced linearly by overburden pressure increase.

- Max$(-\sigma_r)$ depends linearly on the residual cavity gas pressure.

- R_2/a_2 is independent of density, cavity pressure, and overburden pressure.

- r_m/a_2 is restricted to a narrow range that is insensitive to all parameters.

83

A logical next step in the use of the analysis is to derive maximum stress and location formulas for the condition of full cavity contraction.

The next step to improve the analysis is to incorporate a tensile yield strength that is less than the compressive yield strength.

VI REFERENCES

1. R. W. Gates and C. F. Petersen, "A Laboratory Method for Studying Stemming of Line-of-Sight Tunnels in Underground Nuclear Tests," SRI Final Report DNA 3058Z, Contract DNA 001-72-C-0047 (November 1972).

2. R. W. Gates, C. F. Petersen, and A. L. Florence, "Laboratory Method for Studying Stemming of Line-of-Sight Tunnels in Underground Nuclear Tests," SRI Final Report DNA 3592F, Contract DNA 001-73-C-0122 (December 1973).

3. A. L. Florence, "Laboratory Investigation of Stemming of Horizontal Line-of-Sight (HLOS) Underground Nuclear Tests," SRI Final Report DNA 3684F, Contract DNA 001-74-C-0101 (February 1975).

4. A. L. Florence, "Laboratory Investigation of Stemming of Underground Nuclear Test," SRI Interim Report (DRAFT), Contract DNA 001-75-C-0083 (March 1976).

5. A. L. Florence and R. W. Gates, "Dynamic Grout Extrusion Experiments," SRI Topical Report TR-3702-4 (in preparation), Contract DNA 001-75-C-0083.

6. A. L. Florence and R. W. Gates, "Explosive Cavity Residual Stress Experiments," SRI Topical Report TR-3702-3 (in preparation), Contract DNA 001-75-C-0083.

7. A. L. Florence and T. C. Kennedy, "A Simple Analysis for Containment Studies," SRI Topical Report TR 3702-2 (DRAFT), Contract DNA 001-75-C-0083 (August 1976).

8. A. L. Florence, "On the Use of Photomechanics for Containment Studies," SRI Topical Report TR-3702-1 (DRAFT), Contract DNA 001-75-C-0083 (March 1976).

9. D. C. Erlich, "Three-Dimensional Seismic Modeling," SRI Final Report AFCRL-TR-0478, Contract F19628-74-C-0157 (August 1975).

10. H. G. Hopkins, "Dynamic Expansion of Spherical Cavities in Metals," in progress in Solid Mechanics, Vol. I, Chapter III, pp. 85-164, I. N. Sneddon and R. Hill, Eds. (Interscience Publishers, Inc., New York, 1960).

DISTRIBUTION LIST

DEPARTMENT OF DEFENSE

Director
Defense Nuclear Agency
    ATTN: DDST
    ATTN: STSI
3cy   ATTN: STTL

Defense Documentation Center
12cy   ATTN: TC

Commander
Field Command
Defense Nuclear Agency
    ATTN: FCPR
    ATTN: FCTMC, Carl Keller

Chief
Livermore Division, FCDNA
Lawrence Livermore Laboratory
    ATTN: FCPRL

Chief
Test Construction Division
Field Command Test Directorate
Defense Nuclear Agency
    ATTN: Joe LaComb

DEPARTMENT OF THE ARMY

Commander
Harry Diamond Laboratories
    ATTN: DRXDO-NP

DEPARTMENT OF THE NAVY

Commander
Naval Surface Weapons Center
    ATTN: Naval Nuclear Program Office

DEPARTMENT OF THE AIR FORCE

AF Weapons Laboratory, AFSC
    ATTN: SUL

ENERGY RESEARCH & DEVELOPMENT ADMINISTRATION

University of California
Lawrence Livermore Laboratory
    ATTN: David Oakley
    ATTN: Billy Hudson
    ATTN: Mr. Terhune

Los Alamos Scientific Laboratory
    ATTN: Robert Brownlee
    ATTN: Fred App

Sandia Laboratories
    ATTN: Wendell Weart
    ATTN: Lynn Tyler

U.S. Energy Research and Development Administration
Nevada Operations Office
    ATTN: Robert Newman

DEPARTMENT OF DEFENSE CONTRACTORS

General Electric Company
TEMPO-Center for Advanced Studies
    ATTN: DASIAC

Stanford Research Institute
    ATTN: Alex Florence

Pacifica Technology
    ATTN: G. I. Kent

Physics International Company
    ATTN: E. T. Moore

Systems, Science & Software, Incorporated
    ATTN: Russell E. Duff

Terra Tek, Incorporated
    ATTN: Sidney Green